Particle Transpot in ASDEX Upgrade

K.W. Gentle*, O. Gehre, P.T. Lang,
ASDEX-Upgrade, NI and ICRH teams

IPP 1/282 November 1994

MAX–PLANCK–INSTITUT FÜR PLASMAPHYSIK

85748 GARCHING BEI MÜNCHEN

MAX-PLANCK-INSTITUT FÜR PLASMAPHYSIK

GARCHING BEI MÜNCHEN

Particle Transpot in ASDEX Upgrade

K.W. Gentle*, O. Gehre, P.T. Lang,
ASDEX-Upgrade, NI and ICRH teams

IPP 1/282 November 1994

*University of Texas, Austin, USA

Die nachstehende Arbeit wurde im Rahmen des Vertrages zwischen dem Max-Planck-Institut für Plasmaphysik und der Europäischen Atomgemeinschaft über die Zusammenarbeit auf dem Gebiete der Plasmaphysik durchgeführt.

Particle Transport in ASDEX-Upgrade

K.W. Gentle*, O. Gehre, P.T. Lang,
ASDEX-Upgrade, NI and ICRH teams

Particle transport coefficients are estimated by modelling the time evolution of electron density as determined from the ASDEX-Upgrade DCN-interferometer in a variety of discharges. These include L-H transitions for ohmic, ICRF, and beam-heated H-modes, density ramps, and pellet injection. The density evolution can generally be modeled satisfactorily. The inward convection in ASDEX-Upgrade (AUG) is generally rather small, and a D ~ 0.5 m^2/s is required to fit the time evolution. As an equilibrium transport coefficient, this implies rather short particle confinement times; some alternatives are discussed.

I. Introduction

Since the equilibrium density profile offers little insight into particle transport, determination of particle transport coefficients requires time-dependent analysis. Modulated density experiments are a powerful, but specialized technique.[1,2] In principle, any evolution n(r,t) can be analyzed to extract transport coefficients. However, the observed quantity is a chord-integrated density. Given sufficiently many chords of high accuracy, a direct analysis is possible, but often problematic. Especially when the number of chords is limited, as in AUG, an alternative approach is advantageous, that of analytic modeling. In this approach, the transport coefficients D(r,t) and V(r,t) are chosen to have physically reasonable forms with a limited number of adjustable parameters. The parameters are varied, and the model results compared with the observations. The comparisons here will be qualitative, but they could be made quantitative by computing and minimizing the χ^2 error between model and observation. Significance can also be quantitatively evaluated by determining the experimental uncertainties as a χ^2_{exp}, below which improvements are not meaningful. The methodology has been discussed.[1]

This modeling approach has been applied to a number of discharges in AUG to estimate particle transport coefficients. These include L-H transitions under various conditions, density ramps, and pellets. It generally uses the five horizontal channels and the outer vertical channel of the interferometer.(Fig.1) (The other vertical channels are omitted because the contributions to the chord integral from the divertor region are unknown.) Section II discusses the model and analysis technique, Section III gives results for a number of L-H transitions, Section IV shows ohmic density ramps, and Section V discusses a pellet shot. Comments and conclusions follow in Section VI.

*University of Texas, Austin, USA

II. Method

The experimental observations are analyzed by comparing the observed chord integrals with predictions of suitably-chosen transport models. The transport model solves the particle conservation equation in cylindrical coordinates:

$$\frac{\partial n}{\partial t} = \left(\frac{1}{r}\frac{\partial}{\partial r} r\right)\left[D(r,t)\frac{\partial n}{\partial r} + V(r,t)n\right] + S(r,t) \qquad (1)$$

The solution n(r,t) is interpreted as the flux-surface density and coupled with the chord lengths generated from the AUG program fsCUT1 from the corresponding shot and time to generate predictions for each of the interferometer chords. (This is facilitated by converting Eq.(1) to dimensionless coordinates with $\rho = r/a$, $\rho=1$ being the separatrix.) The source term S(r,t) in Eq. (1) comprises two parts, a source within the plasma and a sink representing parallel flow to the divertor outside $\rho = 1$. The source within the plasma is the inhomogeneous term and is written in separable form CS(r)I(t), where S(r) represents the radial profile from neutral penetration, I(t) represents the time variation of the source, which here is approximated by one of the AUG H_α monitors (either HAD DIV or AR13/6) and C is a constant chosen to fit the data at the beginning of the model calculation, usually at t = 1.0 or t = 1.5, after the current has reached its plateau. (The use of an H_α monitor is not quantitatively accurate, for the source S is entirely within the last closed flux surface, and the H_α chords certainly include contributions from outside as well. However, the objective is only to construct a physically plausible, not physically exact, model of the edge region and concentrate on the interior evolution, the chords H-1 to H-5.) For these calculations, S(r) was scaled from Becker's calculations in ASDEX to AUG. Although the radial profile S(r) may change slightly with time as the density evolves during a discharge, it is always localized so strongly at the edge that details do not affect the result. The sink is $-n/\tau_f$, where the characteristic time for flow to a material surface τ_f, could be calculated from estimates of edge temperatures and connection lengths ($\tau_f \sim L/c_s$), but for these calculations was simply adjusted to give a density scale length for $\rho>1.0$ of reasonable value. Equation (1) was solved with a boundary condition n=0 at $\rho=1.05$, but the sink model makes this boundary condition unimportant.

The functional forms for D(r,t) and V(r,t) have been chosen as simple as possible consistent with the inclusion of reasonable physical effects. For the convective velocity,

$$V(\rho) = \rho V_e[\, 1 + \beta(\rho-0.5\,)] \qquad (2)$$

The constant V_e is an effective amplitude, and β allows adjustment of the shape. For most cases, both are constants in time. In a few instances, V_e is ramped linearly between values before and after the L-H transition, but no complex time dependence is employed. The values for D are more complex. For ohmic and L-mode, the form is

$$D(\rho) = D_a \frac{1 + \alpha\rho^2}{1 + 0.5\alpha} \qquad (3)$$

where D_a is an average magnitude and α adjusts the shape. (A value $\alpha \sim 1$ is chosen here in accordance with the radial profiles found for D in ASDEX gas modulation experiments and the general observation that particle transport, like energy transport, increases toward the edge.[2,3]) As with V_e, D_a may have some simple time dependence. The H-mode is modeled by modification of this $D(\rho)$. During H-mode, D is reduced for $\rho > 0.94$. A piecewise linear form for D_e ($\rho > 0.96$) is constructed; the value of D(1) is plotted as part of the model result in subsequent sections. These lower values of D represent the edge barrier. The value of $D(\rho)$ is linearly ramped from the value in Eq(3) to the edge value over the range $0.94 > \rho > 0.96$ to avoid discontinuities. The real edge barrier may be stronger and narrower, but the basic effect, especially as reflected in the chord integrals, can be correctly represented. The only question is whether this model is adequate to represent the outer vertical chord (V-3), but there are several issues there to be discussed with the data.

The values quoted for individual model calculations are generally D_a of Eq. (3) and the (dimensionless) pinch $P = aV_e/D_a$. Particularly for analysis of equilibria, the value of P is rather well prescribed by the density profile. On the other hand, the value of D_a, as will be discussed below, is somewhat uncertain. It depends on the absolute particle confinement time -- the absolute magnitude of the H_α source. In the model calculations, V_e scales directly with D_a to fit a particular set of data and thus P will be insensitive to the choice of D_a.

The solutions of Eq.(1) are computed numerically using a conventional Crank-Nicholson implicit algorithm. The code is written in C and runs adequately on a Macintosh, better on the most modern ones.

The model as described provides good fits to AUG data, including L-H transitions, as will be seen in the following Sections. However, the particle confinement times are rather short, $\tau_p < 20$ ms. An alternative formulation, motivated partly by the usual linearization procedure for small perturbations to an equilibrium but generalized here as a purely phenomenological model, separates $n(r,t)$ into two parts, $n(r,t) = n_{eq}(r,t) + n_\Delta(r,t)$, where $n_{eq}(r,t)$ is the solution to the inhomogeneous ordinary differential equation

$$D_{eq}(r,t)\frac{dn_{eq}}{dr} + V_{eq}(r,t)n_{eq} = -\frac{1}{r}\int_0^r S(r',t)\, r'dr' \qquad (4)$$

The partial differential equation for $n_\Delta(r,t)$ becomes

$$\frac{\partial n_\Delta}{\partial t} = \left(\frac{1}{r}\frac{\partial}{\partial r}\, r\right)\left[D(r,t)\frac{\partial n_\Delta}{\partial r} + V(r,t)n_\Delta\right] - \frac{\partial n_{eq}}{\partial t} \qquad (5)$$

However, the transport coefficients in Eq.(5) can be different from those of Eq.(4), a feature emphasized by the labels D_{eq},V_{eq}. Such effects are inevitable in linearization if the transport coefficients are nonlinear in the local variables, but they are applied here without constraining $n_\Delta << n_{eq}$. The *a posteriori* justification of Eq.(5) as a possible linearization of Eq.(1) will be discussed with the specific examples for which Eqs. (4-5) are used to model the experiment.

For reference, the dimensionless equations are given below. The choice has some physical consequences because it determines the dimensional magnitude of quantities inferred from the dimensionless values of the model. For example, the dimensionless "D" scales with a^2 to the physical value. For circular cross-sections, a is the radius, but for elongated plasmas, $a\sqrt{\kappa} = \sqrt{(ab)}$ is probably more appropriate.

The dimensions are removed by converting to variables $\rho = r/a$ and $\tau = t/\tau_c$, where $\tau_c = a^2/D_o$, with D_o being an arbitrary reference value for D, usually 1 m^2/s here. For convenience, a reference value V_o is also chosen. The dimensions of n are not removed; it is assumed to be in units of 10^{19} m^{-3}, which is convenient for comparing with experiment. Units do not matter in homogenous equations, like Eq.(5), but for Eqs. (1) and (4), S is assumed to have the same density units, reflected in C. Quantities like particle confinement times, being quotients, are independent of C and density units. The Eqs.(1,4,5) become

$$\frac{\partial n}{\partial \tau} = \left(\frac{1}{\rho}\frac{\partial}{\partial \rho}\rho\right)\left[d(\rho,t)\frac{\partial n}{\partial \rho} + v(\rho,t)P_o n\right] + \tau_c S(\rho,t) \qquad (6)$$

$$d_{eq}(\rho,t)\frac{dn_{eq}}{d\rho} + v_{eq}(\rho,t)P_o n_{eq} = -\frac{1}{\rho}\int_0^\rho \tau_c S(\rho',t)\,\rho' d\rho' \qquad (7)$$

$$\frac{\partial n_\Delta}{\partial \tau} = \left(\frac{1}{\rho}\frac{\partial}{\partial \rho}\rho\right)\left[d(\rho,t)\frac{\partial n_\Delta}{\partial \rho} + v(\rho,t)P_o n_\Delta\right] - \frac{\partial n_{eq}}{\partial \tau} \qquad (8)$$

$$\tau_p = \frac{\int_0^a n\, r\, dr}{\int_0^a S\, r\, dr} = \frac{\int_0^1 n\, \rho\, d\rho}{\int_0^1 S\, \rho\, d\rho} \qquad (9)$$

where $d(\rho,t) = D(\rho,t)/D_o$, $v(\rho,t) = V(\rho,t)/V_o$, and $P_o = aV_o/D_o$. (Although the equation is solved in dimensionless units, specified functions like $D(\rho,t)$ retain the physical time,

which must also be carried in the calculation for comparison with the data, as the more convenient variable.)

III. First L-H transitions

This analysis approach has been applied to several ohmic, ICRH, and beam-heated H-modes. The initial examples were at 800 kA and beam powers up to 5 MW. The ohmic and ICRH examples were specially interesting because there was no core fueling to affect the result.

Shot 2703 is an ohmic H-mode at $B_T = 1.2$ T with good plateaus before and after the transition that has been extensively modeled. If one uses a D_a somewhat smaller than obtained from gas modulation experiments on ASDEX, as befits a larger machine, adjusts V_e to fit the ohmic profile before transition, and imposes an edge barrier which reproduces the edge channels, the result is that of Fig. 2. The experimental traces are shown in heavy lines and the model results in thin lines, a convention used throughout. For this case, $D_a = 0.06$ m^2/s and $P \sim 0.1$, giving a particle confinement time of ~ 100 ms. The model agrees with experiment before the L-H transition. The edge barrier, D(a,t) as plotted, is sufficient to give good agreement for the edge interferometer channel (V-3), but the density does not rise fast enough for any of the interior channels (H-1 through H-5). In the model, the density at the center does not increase significantly, and the profiles become quite hollow after the transition. The results for $n(\rho,t)$ are shown in Fig. 3, with times referenced to the L-H transition. To match the observations, particles must reach the center.

In principle, an increase in either D or V could provide this. Increasing D and V together, keeping P fixed, would suffice, but the particle confinement time would then decrease greatly, as noted below. Alternatively, values of D or V different from the equilibrium ones could be used for the perturbation. An increase of V must be restricted to the perturbation, otherwise the profile will peak, contrary to the observations. The result from a model using the equilibrium transport coefficients of Fig. 2 but a $D = 0.5$ m^2/s for the perturbation is shown in Fig. 4. The edge barrier is modified slightly from Fig. 2 to maintain the good edge fit. This model provides a good fit to all the channels. The value of D is reasonably well determined: variations of ±25% produce models with clearly inferior fits to the data. The corresponding results for $n(\rho,t)$ are shown as Fig. 5. Very little hollowness is required to drive density to the center with this value of D.

(Figure 4 illustrates one detail common in much of this analysis. The two interferometer channels H-4 and H-5 are clearly separate in the data, but the model predicts almost the same values. This is not a fault of the model. The magnetic geometry indicates that the two channels view nearly the same flux surfaces; a density dependent only on flux surface should give no significant differences between the two channels. Either the density is not constant on flux surfaces or there is some error in the reconstruction of the magnetic configuration.)

Instead of using $D = 0.5$ m^2/s only for the perturbation, one could take this value as D_a, keep P fixed, and obtain an equally good fit to the observations. However, the particle

confinement time would be ~ 10 ms, a rather small value for a machine the size of AUG. On the other hand, a difference of almost a factor of ten between the equilibrium and perturbation transport coefficient is also rather large. The transport coefficients are depicted in Fig. 5. The H-mode edge barrier nearly doubles the particle confinement time. As one might expect from Fig. 5, the densities are never far from their equilibrium values. In the notation of Eqs. (6-8), $n_\Delta << n_{eq}$. For the calculation of Figs. 3-4, $|n_\Delta / n_{eq}| < 0.2$, even at the edge just after the L-H transition. One could thus regard the enhanced $d(\rho,t)$ in Eq.(8) as the result of linearizing Eq.(6), hypothesizing a strong nonlinearity.

One alternative is to retain $D_a = 0.06$ m^2/s but enhance the inward convection for the perturbation -- $v(\rho,t)$ in Eq. (8). A reasonable fit for this case is shown in Fig. 7, but a value of $V_e \sim 1$ m/s is required. Although this is not a large value compared with results for some cases in ASDEX or TEXT, it is certainly much larger than the $V_e \sim 0.01$ m/s characteristic of the equilibrium. Furthermore, $V_e \sim 1$ m/s is not plausible as an equilibrium pinch. The profile shape requires $P \sim 0.1$, and D would thus have to exceed 10 m^2/s. However, it is comparatively easy to obtain a V in Eq. (5) for the perturbation that is much different from the V in Eq. (4) for the equilibrium. Several off-diagonal terms could sum up to give the equilibrium V, and numerous terms appear in the V of Eq. (5).[4] This contrasts with the result for D, in which only a nonlinear dependence of D on $\partial n/\partial r$ gives a D for perturbations different from the D for equilibrium. Regardless of model, the density evolution following the L-H transition requires transport coefficients which are either much different from the equilibrium ones or imply short particle confinement times.

A second example of an ohmic H-mode is shown in Fig. 8 for shot 2704. For this calculation, $D_a = 0.06$ m^2/s , $P = 0.2$, and an enhanced $D = 0.3$ m^2/s was used, values generally similar to those of Fig. 4.

An ICRH H-mode is illustrated in Fig. 9 for shot 2850 at $B_T = 2.0$ T. The initial equilibrium uses $D_a = 0.06$ m^2/s and $P = 0.15$ with an enhanced $D = 0.5$ m^2/s for the perturbation, very similar to the values of Fig. 4. The model attempts to follow the evolution through the full L-H-L cycle. The initial relaxation in density following the H-L transition at $t \sim 2.7$ is fit well by the model, but the later evolution is not. The failure is not caused by intrinsic physics but by complexity of detail. Shortly after the H-L transition, the H_α signal becomes very irregular with large, erratic spikes. The simple sort of model used here becomes inadequate to treat the complexity of the actual discharge, which may even be attempting to enter an ohmic H-mode. However, the good fit to the initial relaxation is significant, for it contrasts with the results of other models, as shown below.

To emphasize the need for enhanced transport to explain the transition, Fig. 10 is a model of shot 2850 using the equilibrium transport coefficients of Fig. 9, but with the edge barrier adjusted so that the H-4 and H-5 channels fit the experiment. Note that this requires somewhat lower values of D(separatrix) and that the edge V-3 channel is too large in the model. Nevertheless, the interior channels in the model rise too slowly at L-H and fall too slowly at H-L.

A comparison of enhanced V with enhanced D for the perturbation is provided by Fig. 11. The model fit of Fig. 11 for the L-H transition is approximately as good as Fig. 9. However, the H-L fit is worse for Fig. 11. The decay in channels H-3 to H-5 is clearly too slow. This is the only direct evidence favoring enhanced D over enhanced V as the mechanism for fast profile relaxation.

A second example of an ICRH H-mode with full L-H-L evolution is shown in Fig. 12 for shot 2938, again at $B_T = 2.0$ T The transport coefficients are the same as for the previous ICRH case of Fig. 9.

The beam-heated cases begin with a 1 MW example, shot 3340 at $B_T = 1.36$ T. Figure 13 shows the model fit, which includes the beam particle source, for transport coefficients $D_a = 0.06$ m^2/s and $P = 0.1$ with an enhanced $D = 0.45$ m^2/s for the perturbation. As an example of the sensitivity to enhanced D, Figure 14 shows the model calculated using $D = 0.3$ m^2/s. The fit is clearly much worse. Again, the model attempts to follow the complete L-H-L evolution, but it fails soon after the return to L. The failure is easily understood from the H_α signal. Although the discharge returns to L-mode after termination of the beam, it soon attempts to enter an ohmic H-mode, with large excursions in H_α. The fact that the model gives the same initial slopes for the density relaxation as are observed at the termination of the H phase is as much as can be expected.

A second example at 1 MW is provided by shot 3348 at $B_T = 1.7$ T, shown in Fig. 15. The transport coefficients are $D_a = 0.06$ m^2/s and $P = 0.2$ with an enhanced $D = 0.3$ m^2/s, although $P \sim 0$ in the H phase.

A higher beam power, 2.5 MW, is illustrated in Fig. 16 for shot 3496 at $B_T = 2.0$ T. The initial transport coefficients are $D_a = 0.06$ m^2/s and $P = 0.2$ with an enhanced $D = 0.35$ m^2/s for the perturbation, but $D_a = 0.09$ m^2/s and $P \sim 0.0$ are needed to describe the equilibrium in the presence of the beam. This is the first example in which there are indications of power degradation of the equilibrium transport coefficients, a typical sort of L-mode effect. In gas modulation experiments on ASDEX, the H-mode produced some sort of edge barrier and increase in V, but did not restore D to its ohmic value.

The highest beam power of the early H-mode sequence was 5 MW, shown in Fig. 17 for shot 3703 at $B_T = 2.0$ T and a plasma current of 1.2 MA. Effects were sufficiently strong that the H-2 and H-3 channels were lost; fringe jumps in V-3 at 2.55 and 2.75 are clear. The transport coefficients were $D_a = 0.06$ m^2/s and $P = 0.1$ with an enhanced $D = 0.25$ m^2/s for the perturbation, a somewhat smaller value being required because the beam particle source contributes to the density rise. The fit to V-3 is rather poor in absolute value, but the tangent radius of V-3 from the magnetics is $\rho \sim 0.95$. The result from the model is thus very sensitive both to the exact value of ρ and the form of edge barrier in the model. There are several instances in which changing the tangent radius ± 0.02 of V-3 in the model significantly improved the fit, but whether this represents a fault of the magnetics or the edge barrier model cannot be determined. There is certainly much interesting physics in this region to be explored, but a different diagnostic for density would be required.

IV. Density ramps

Ohmic density ramps from shots 3674 at $B_T = 2.4$ T and 3675 at $B_T = 1.7$ T, both at 1 MA, have been analyzed. The first case is shown in Fig. 18 with transport coefficients $D_a = 0.06$ m^2/s, P = 0.2, and D = 0.6 m^2/s for the perturbation. (For Fig. 18, the equilibrium coefficients were ramped to $D_a = 0.12$ m^2/s and P = 0.1 by the end of the ramp, but as noted previously, that may represent a real transport degradation or merely increased recycling in the divertor region contributing to the H_α signal.) Although the fits to the ramp are not extremely good in following details in the density evolution, probably reflecting subtleties in the evolution of D and V during the shot that the model does not include, sensitivity studies like that between Figs. 13 and 14 confirm that a D ~ 0.6 m^2/s is needed to reproduce the general density increase and avoid large deviations from the observations. The second ramp is shown in Fig. 19. A D = 0.4 m^2/s is required for the perturbation, and the equilibrium coefficients vary from $D_a = 0.06$ m^2/s and P = 0.2 at the start to $D_a = 0.24$ m^2/s and P = 0.2 at the end.

In general, the ohmic density ramps require the same magnitudes of particle transport coefficients as do the L-H-L transitions to explain the time evolution.

V. A Pellet Shot

An excellent example of multiple pellet injection is found in shot 2725. The modeling is shown in Figs 20-22. The large value of D = 0.6 m^2/s was used throughout with P rising from 0.5 before injection to 2.0 at the end. The particle confinement times are therefore rather small, increasing from 20 ms to 33 ms, and the values of P are much larger that the cases above. The pellets are added to the model as delta functions with an ablation profile adopted from the experiment and total amplitude chosen to fit the typical increment in the central interferometer channel. The pellet size from this criterion is consistent with direct estimates of the pellet size. The general agreement in Fig. 20 seems reasonable. The relaxation between pellets matches observations. The general density rise during the series of pellets is not directly caused by particle accumulation but by the increasing source, indicated by H_α, during the discharge. There is gas accumulation in the divertor more than particle accumulation in the plasma.

Examination of the details in Figs. 21 and 22 shows some systematic problems. Although the central H-1 channel is reasonable, problems arise in various outer channels. In Fig. 21, the model H-4 has too large and sharp a peak. In Fig. 22, all channels rise too sharply, and the amplitude of H-3 is too large. The major discrepancies are not caused by the transport model; they are features of the pellet. Since the pellets certainly ablate rapidly (within 1.2 ms) and the interferometer has 1 ms resolution, the slow rise-times observed may indicate flux-surface equilibration times. The pellet density is deposited on flux tubes that may not intersect the interferometer chords and might require tens of milliseconds to diffuse over the flux surface. A more serious problem is that the density increments at each pellet injection cannot be matched for all channels, as can be seen in Figs. 21 and 22.

These increments are determined by the pellet deposition profile, not by transport. The problem is quantified in Fig. 23, which shows the pellet deposition profile used in the model compared with a simple Abel inversion (using spline fits) of the average density increments of the pellets. (The y axis, in arbitrary units, is different for the two curves; only the differences in shape are significant.) The density increments observed imply significant central deposition. One resolution would be multi-step charge exchange, which could provide neutrals promptly in the core. Such a process has been proposed in pellet injection to explain the rapid drop in central temperature sometimes observed in advance of pellet arrival or in the absence of central penetration.

VI. Stronger L-H transitions

Discharges at higher currents and higher heating powers show stronger L-H transitions and other interesting phenomena, like ELM-free periods. Some of these have been analyzed for particle transport effects, but the results are generally similar to those above.

Figure 24 shows results from shot 4741, a 1 MA shot at 2 T with 1.4 MW of ICRH. The density evolution is complex because the ICRH power decreased for a short period near 2.2 sec before returning to its full value and turning off at 2.3 sec. The model, using $D_a = 0.06$ m^2/s and $P = 0.2$, decreasing to $P = 0.1$ in H-mode, with $D = 0.4$ for perturbations, provides a good fit throughout. Following the details of the waveform requires only small modulation of the edge barrier, which stops improving when the heating power drops and gradually weakens after ICRH termination at 2.3 sec. The effects are indicated by the cross-hatched line for D(1.0,t) in Fig. 24.

A second example is provided by shot 4744 in Figs. 25 and 26. In this case, the ELMing H-mode is interspersed with ELM-free phases, during which the density rises more steeply. The model for this case only attempts to follow the evolution through the second ELM-free period, which terminates slightly after 3.2 sec. The fit of Fig. 25 is quite good until after 3.2 sec, using the same transport coefficients as above for shot 4741. The only difference between the shots is the edge barrier. The barrier is stronger (edge diffusion smaller) for shot 4744, especially during the ELM-free periods. The fit to the edge channel -- V-3 -- is not very good in Fig. 25, but if the channel is moved from $\rho = 0.95$, as determined from the flux-surface reconstruction, to $\rho = 0.94$, the much-improved fit of Fig. 26 is obtained. This does not imply a problem with the magnetics; it may mean simply that the edge barrier used in the model, which develops between $0.94 < \rho < 0.96$ and extends to the edge, should be moved to larger ρ. As discussed above, these measurements are not suitable for inferring details of the H-mode edge. The important conclusion is that the model is adequate to reproduce the internal density evolution following ELM effects. To within the accuracy and resolution of this data, no peculiar or nonlocal effects need be invoked. Only a value of $D \sim 0.5$ m^2/s for perturbations is needed. It remains consistent *a posteriori* to consider it the D in a linearized equation for the density perturbation; $\Delta n/n_{eq} \leq 0.3$ at all positions and times for this shot.

Several shots, such as 3500 and 4744, exhibit some large, isolated ELMs with clear signals on all the interferometer channels. However, the ELM does not seem to produce a useful density perturbation. The signals on all channels are simply those expected from a loss of edge density; there are no delayed effects evident on the inner channels. The edge density recovers quickly without significant inward propagation.

VII. Conclusions

Analysis of density transients in AUG suggests that a $D \sim 0.5\ m^2/s$ suffices to describe the temporal evolution. Equilibrium profiles indicate low values of inward convection; it is not necessary to invoke significant V for any case, although conversely, it cannot be excluded. Of course, this analysis excludes the details of the H-mode edge barrier, $0.9 < \rho \leq 1.0$, and any special effects which may occur there.

The question of whether this $D \sim 0.5\ m^2/s$ represents the total D for particle transport or an enhanced value for perturbations about equilibrium cannot be resolved within the context of this analysis. Either possibility is acceptable. Absolute measurements of the ionization source within the last closed flux surface are required to discriminate between the two.

1. K.W. Gentle, O. Gehre, and K. Krieger, " Determination of Particle Transport Coefficients in ASDEX by Gas Modulation," Nuclear Fusion **32**, 217-237 (1992).
2. P.C. Efthimion et al, "Observation of Temperature-Dependent Transport in the TFTR Tokamak," Phys. Rev. Letters **66**, 421 (1991).
3. E.J. Synakowski et al., "Helium, Iron, and Electron Particle Transport and Energy Transport Studies on TFTR," Phys. Fluids B **5**, 2215 (1993).
4. K.W. Gentle, "Dependence of Heat Pulse Propagation on Transport Mechanisms: Consequences of nonconstant transport coefficients," Phys. Fluids **31**, 1105-1110 (1988).

DCN

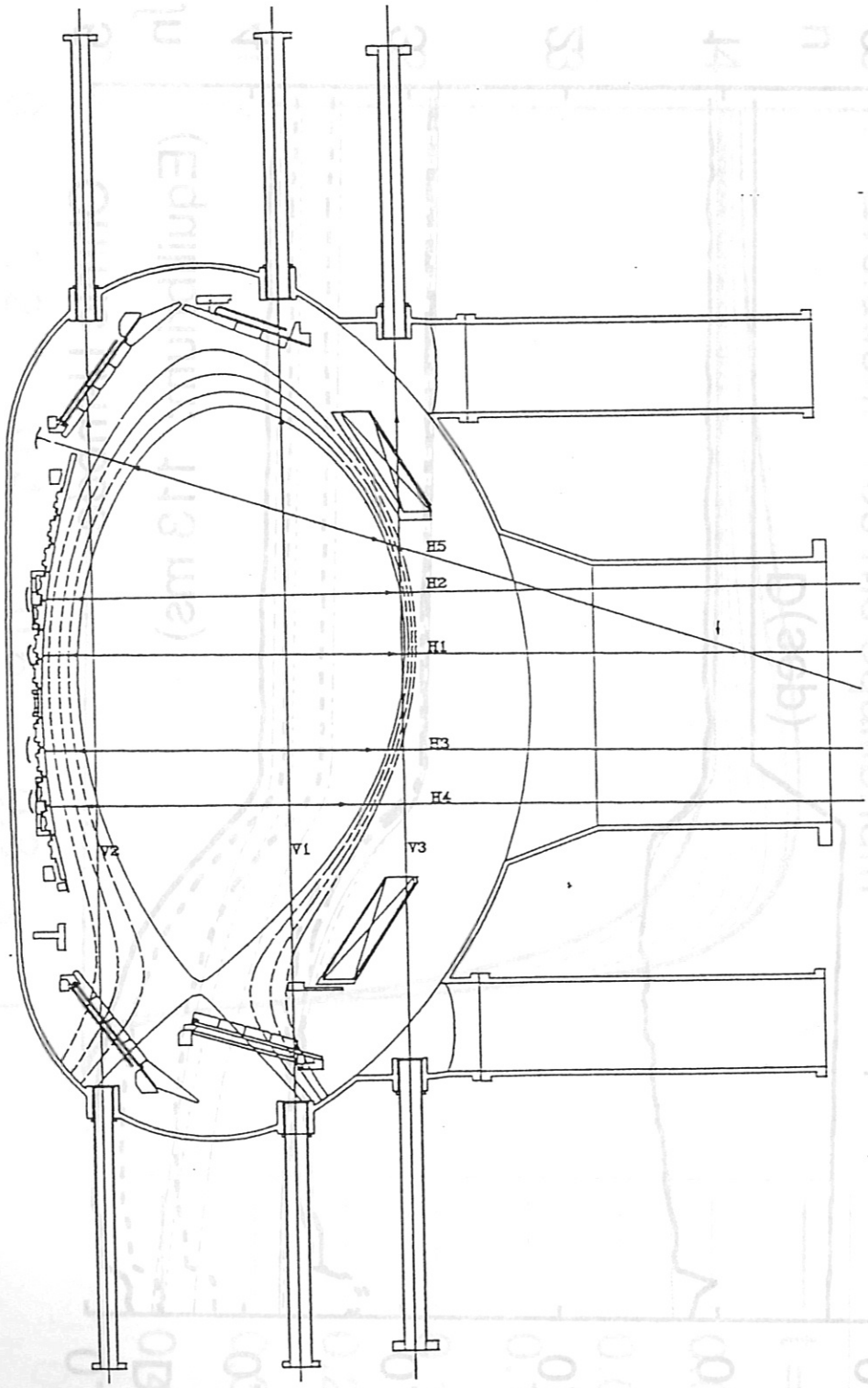

Fig. 1

A2703.CHT.D0;2

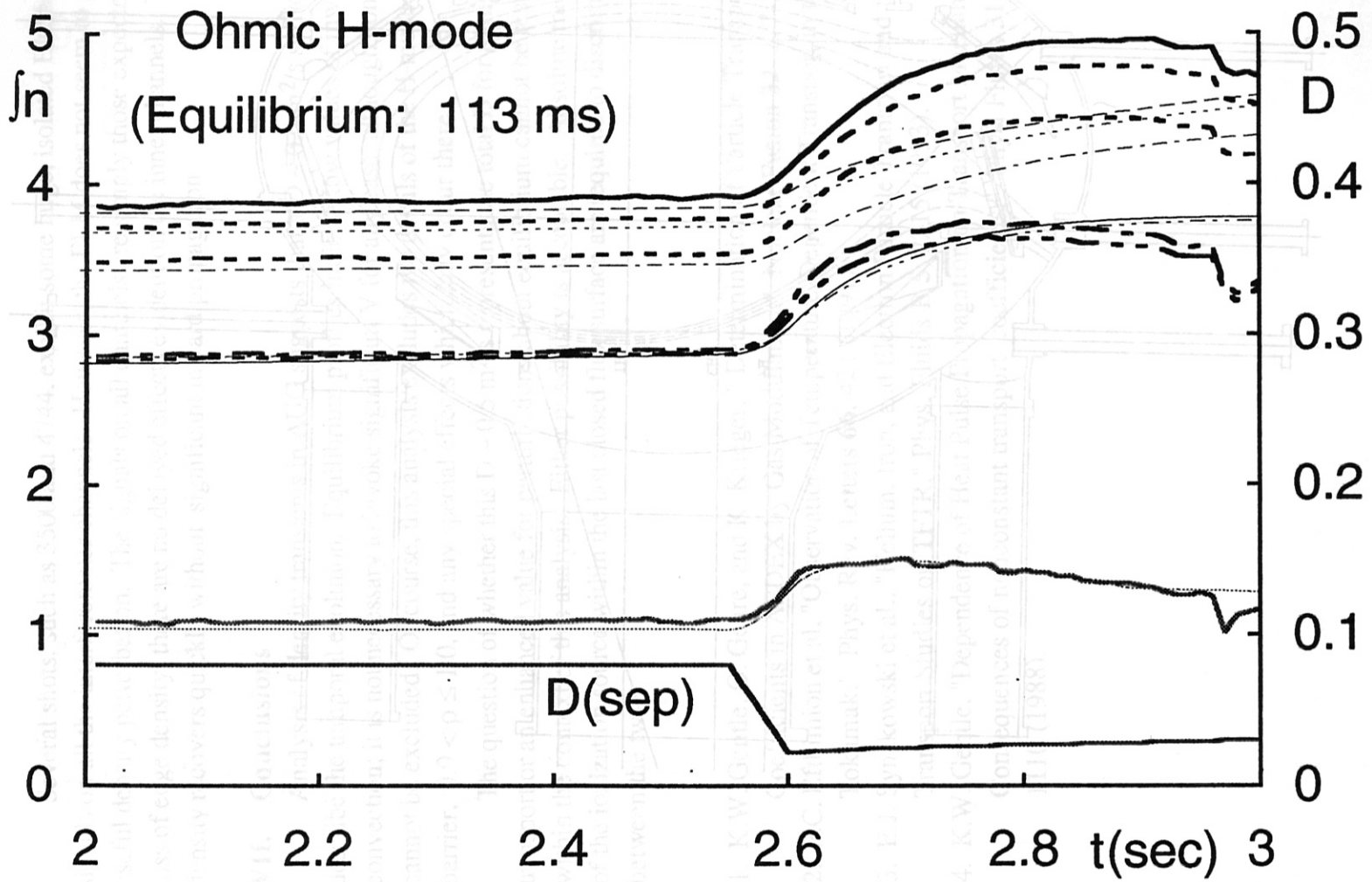

Fig. 2

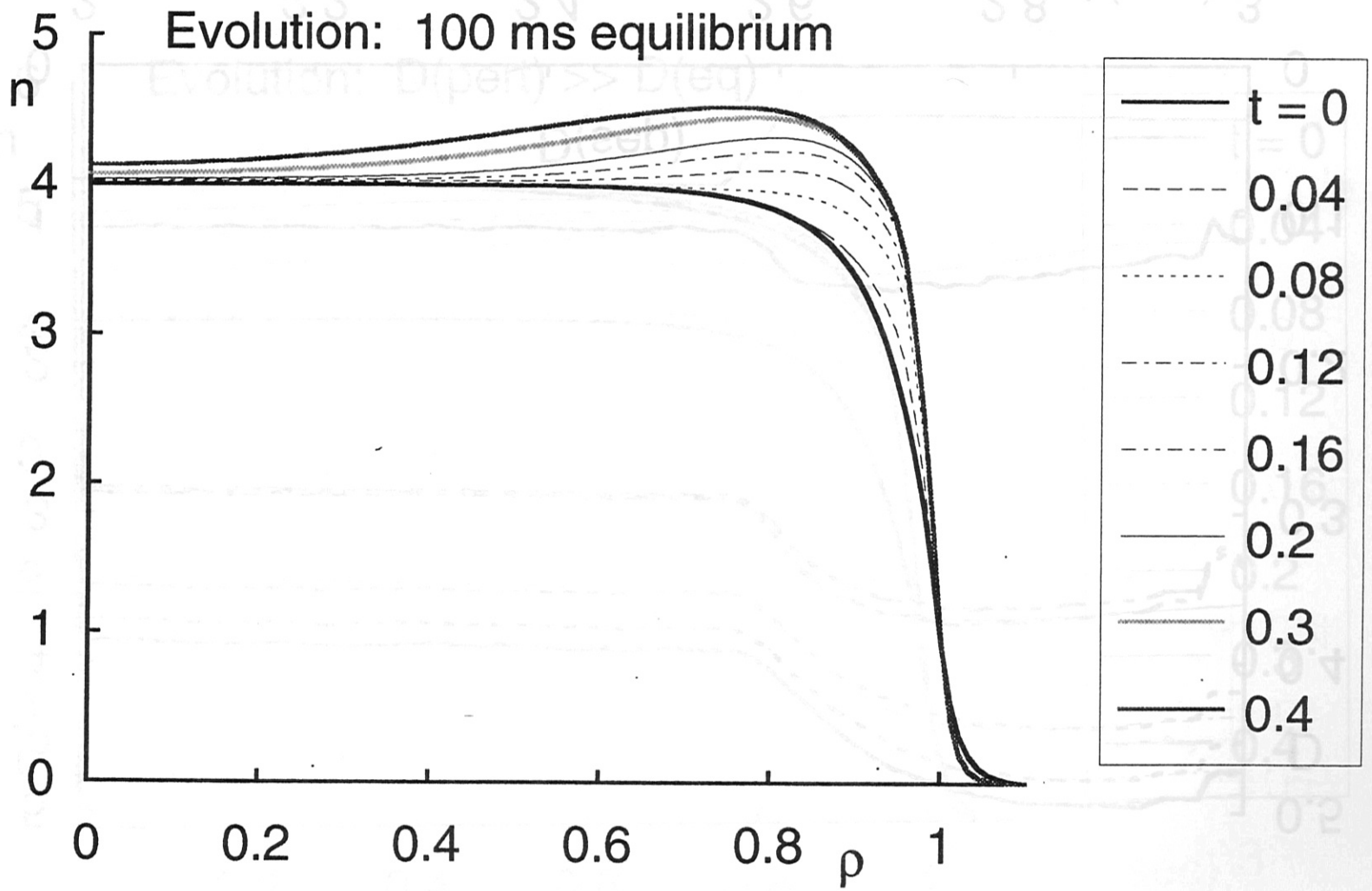
Evolution: 100 ms equilibrium
n
5
4
3
2
1
0
0
0.2
0.4
0.6
0.8
ρ
1
t = 0
0.04
0.08
0.12
0.16
0.2
0.3
0.4

Fig. 3

A2703.CHT1;4

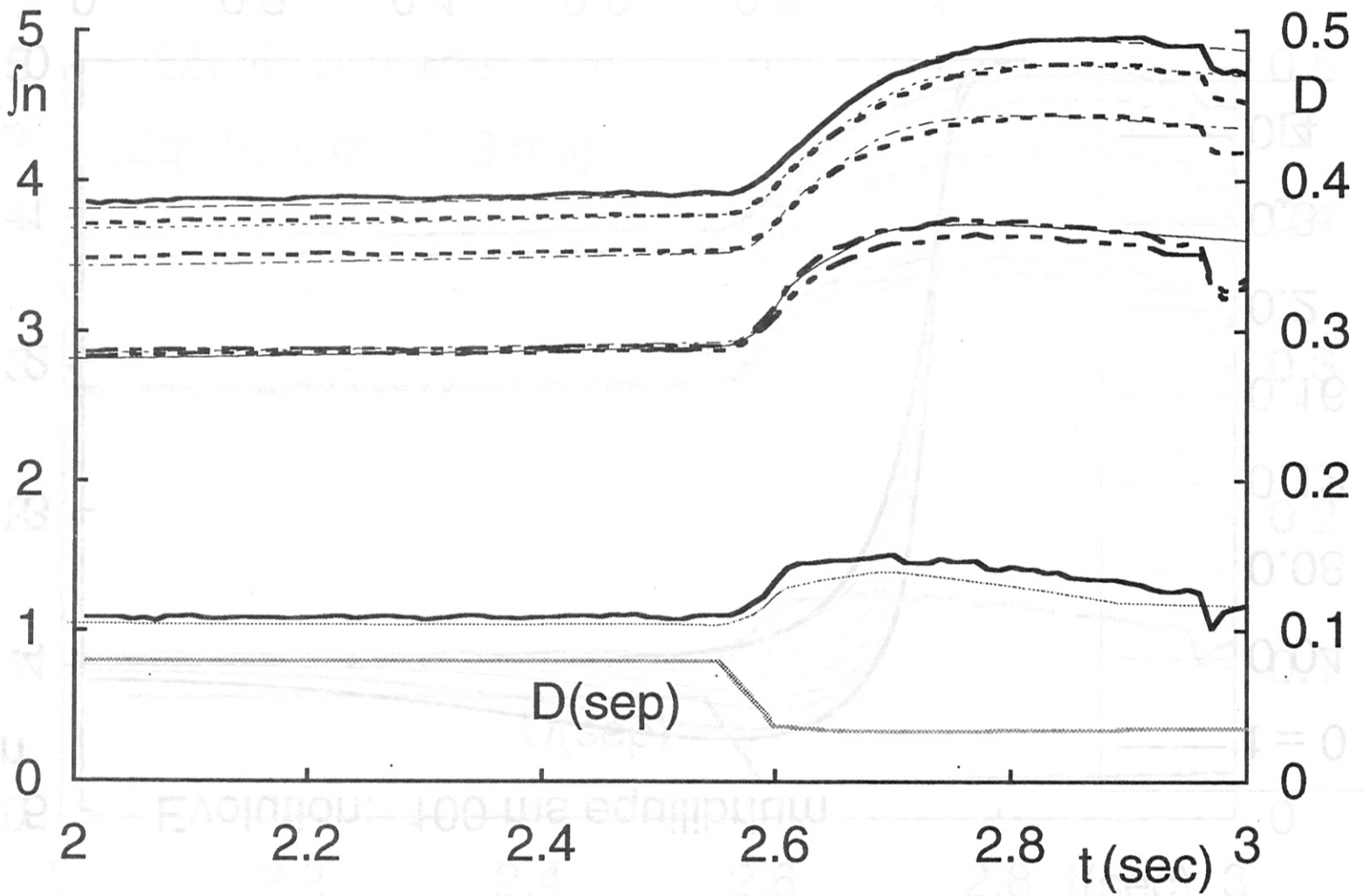

Fig. 4

A2703.CHT.n(t);5

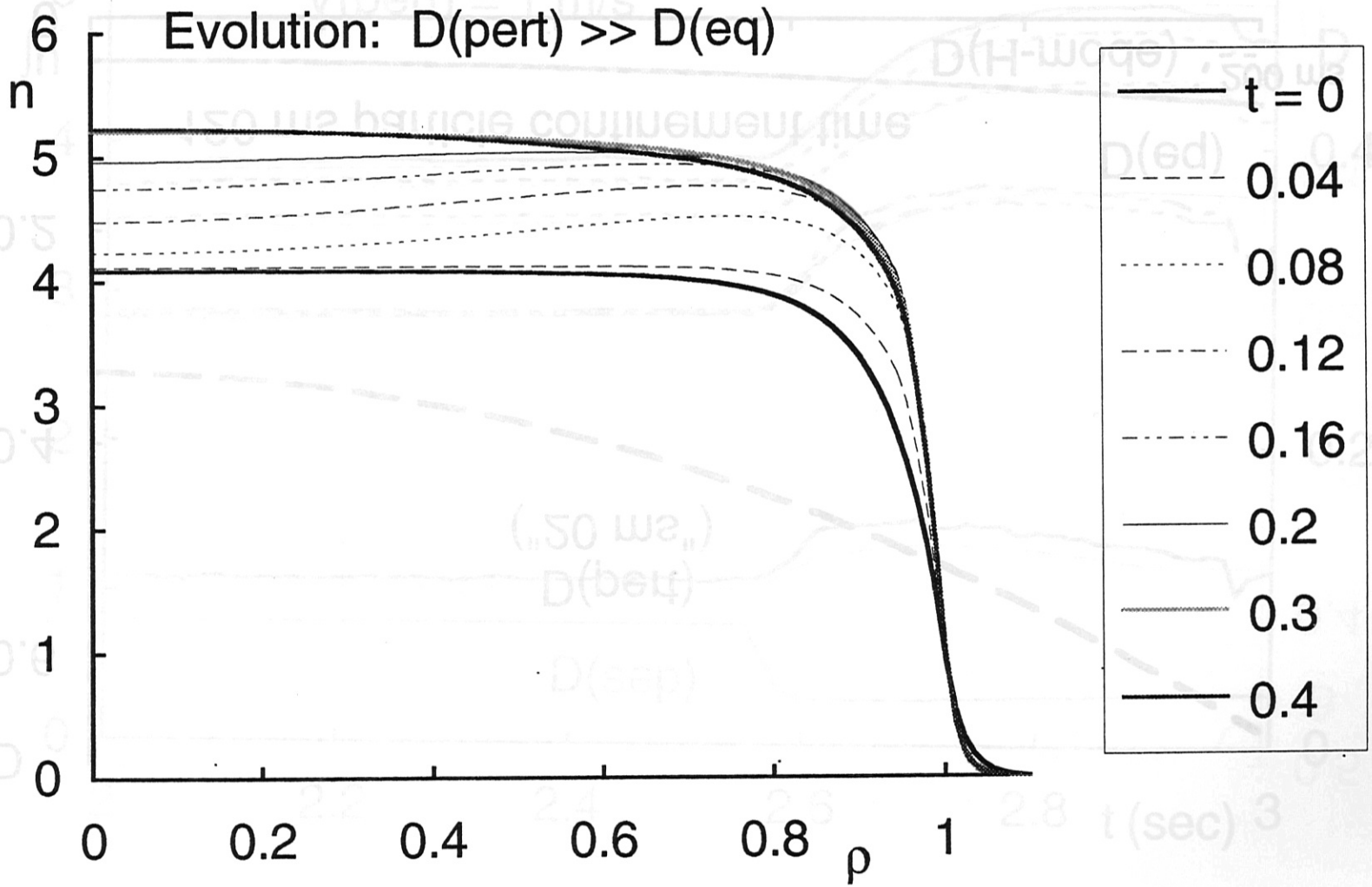

Fig. 5

A2703.CHT.D(r);6

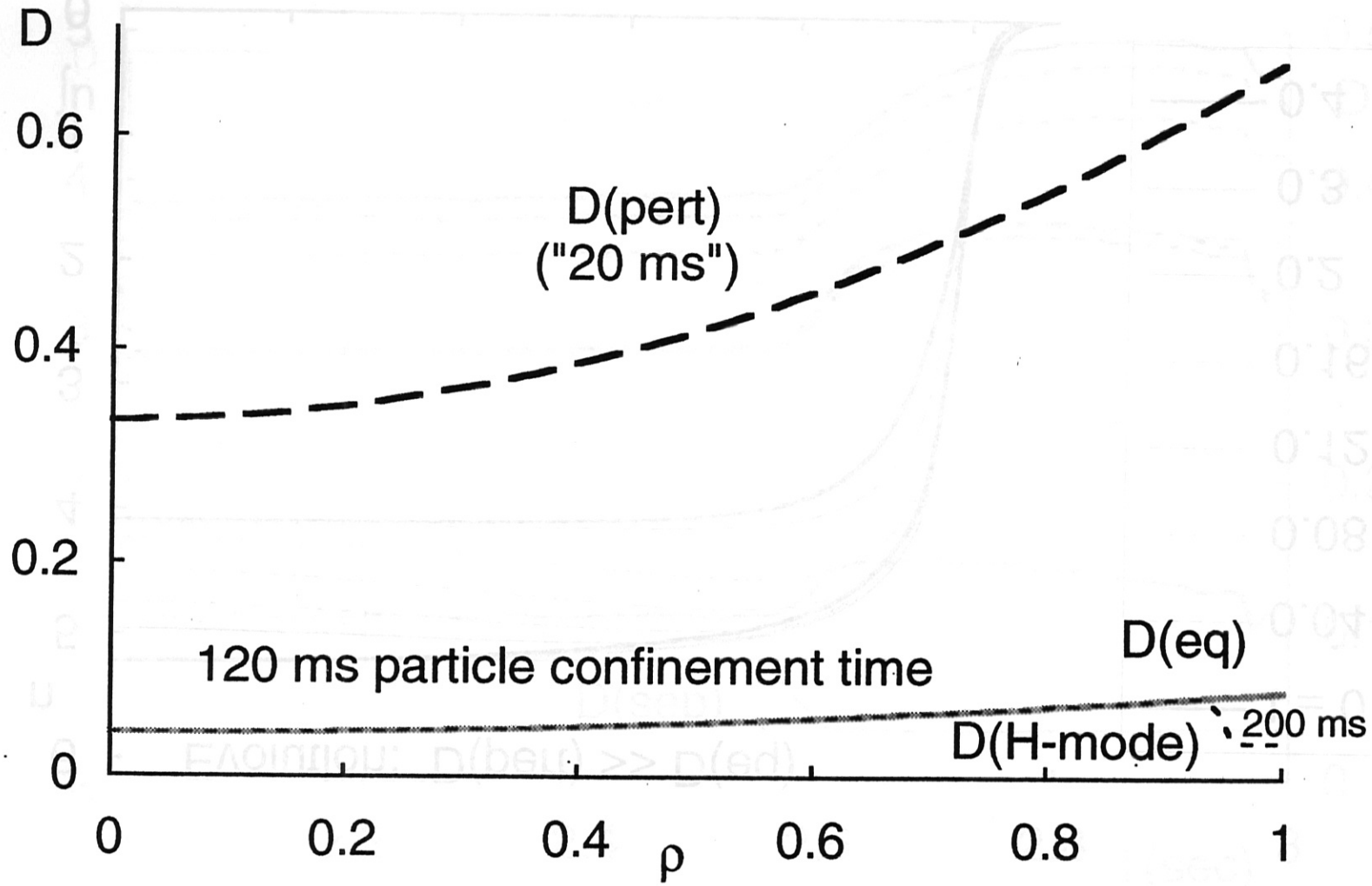

Fig. 6

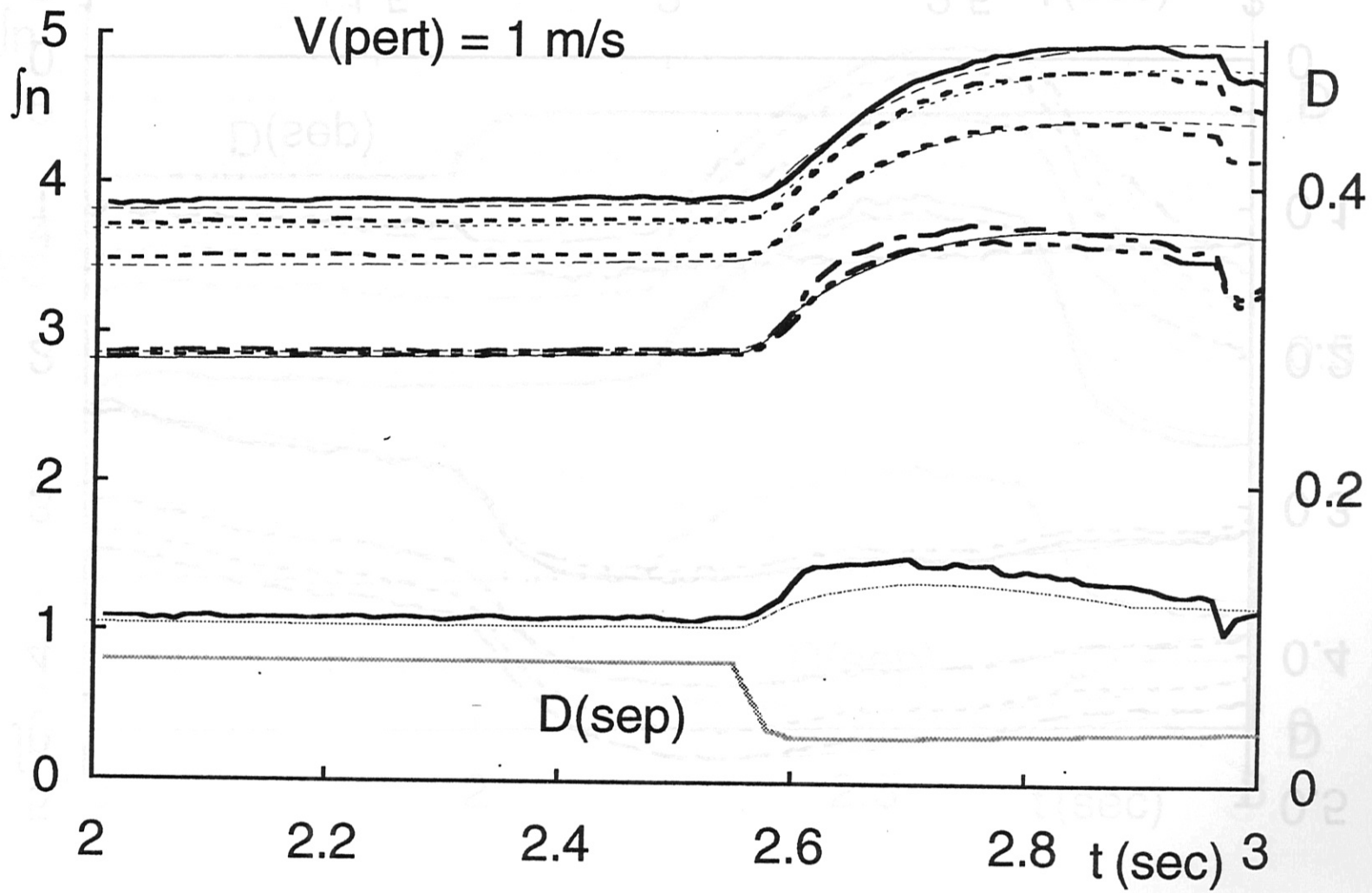

Fig. 7

A2704.CHT1;8

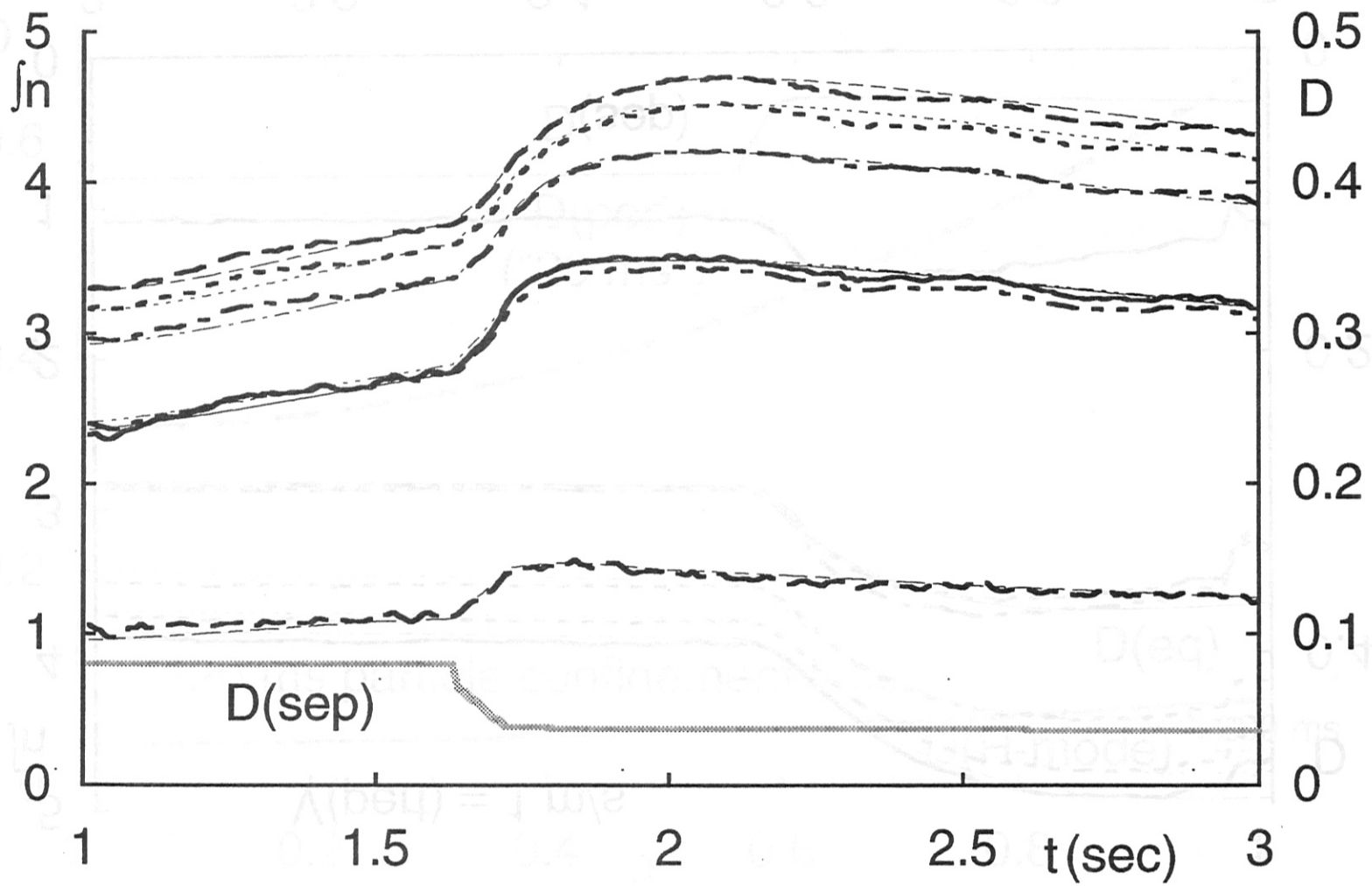

Fig. 8

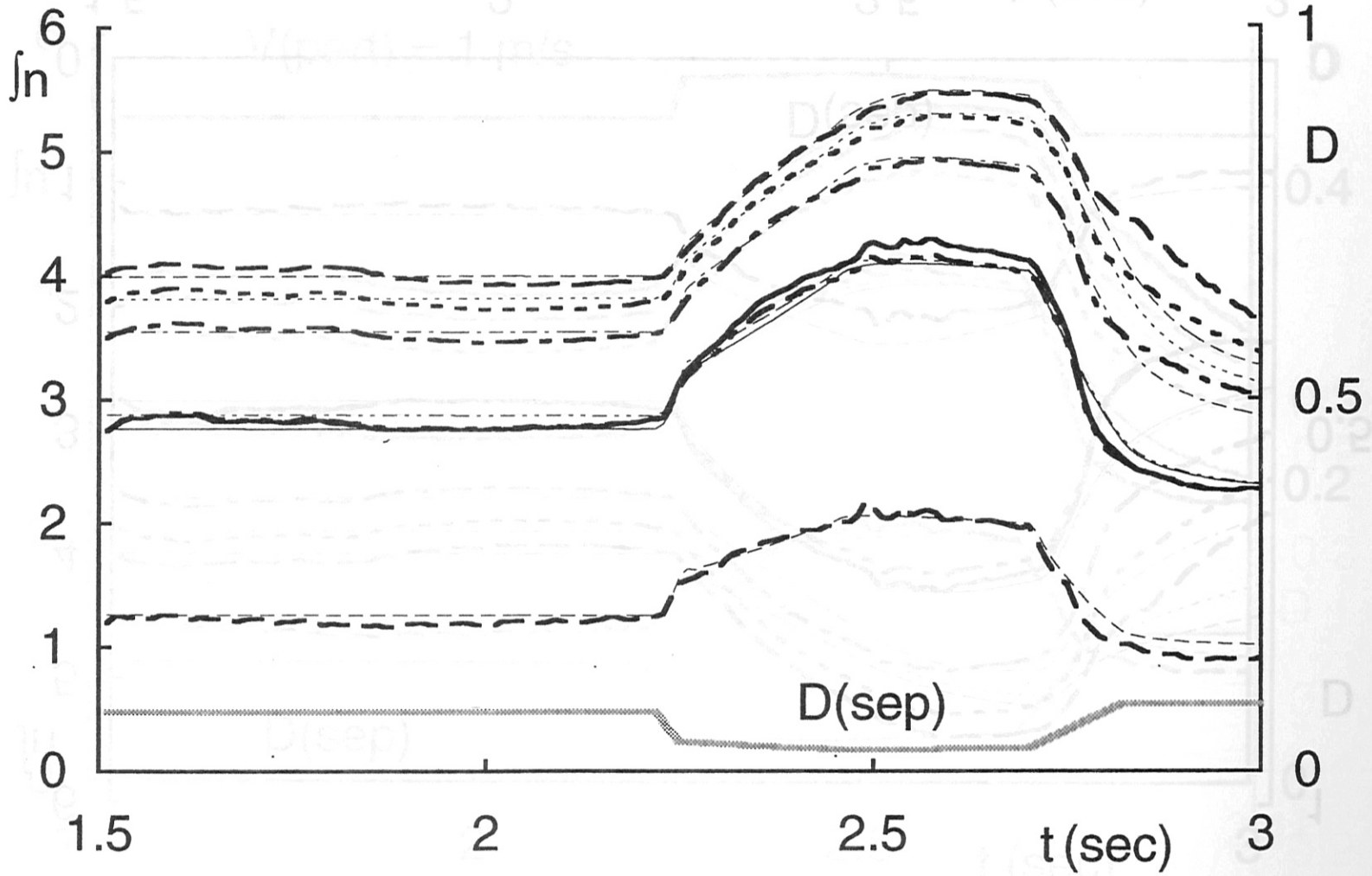

Fig. 9

A2850.CHT2;10

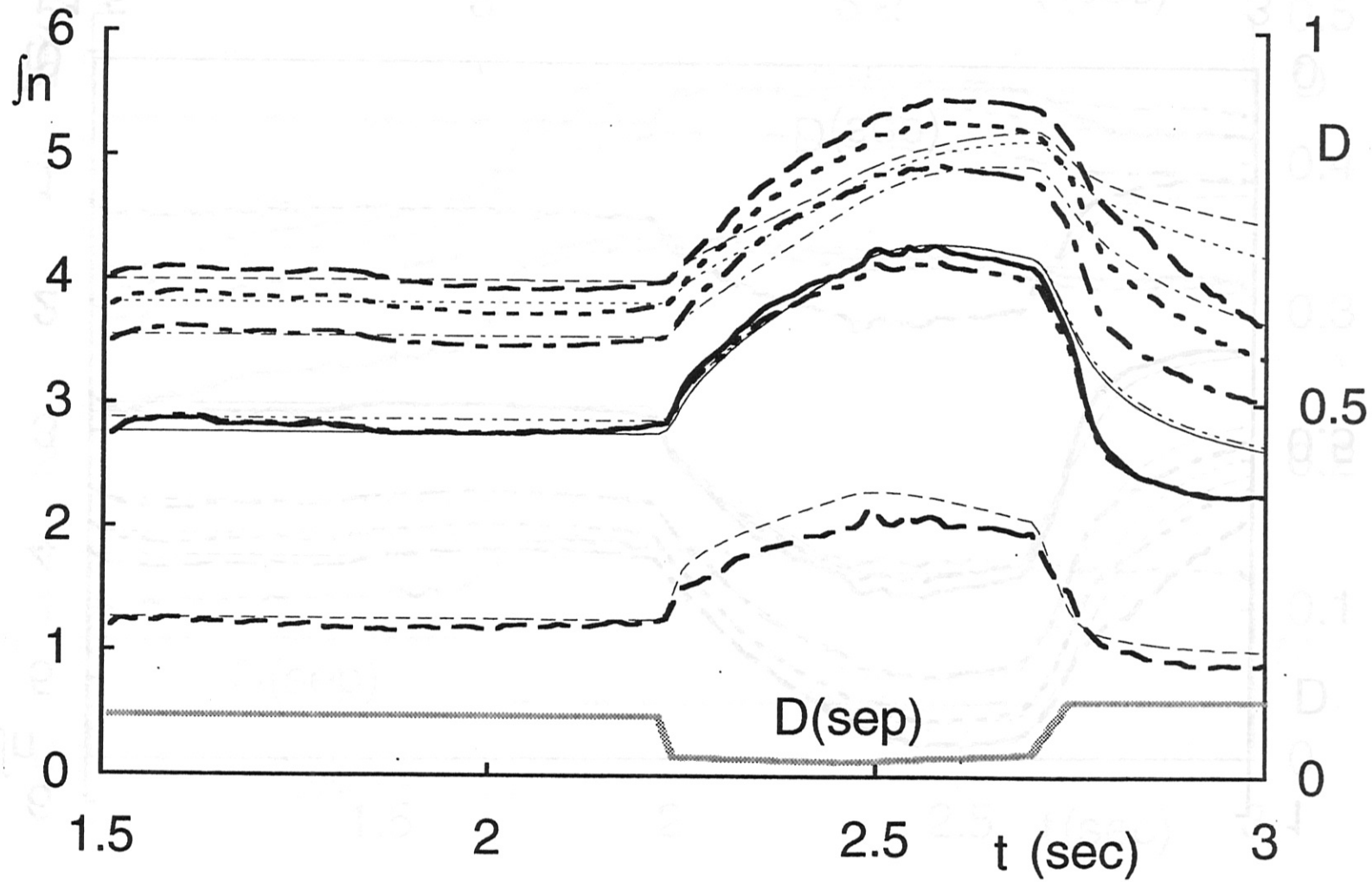

Fig. 10

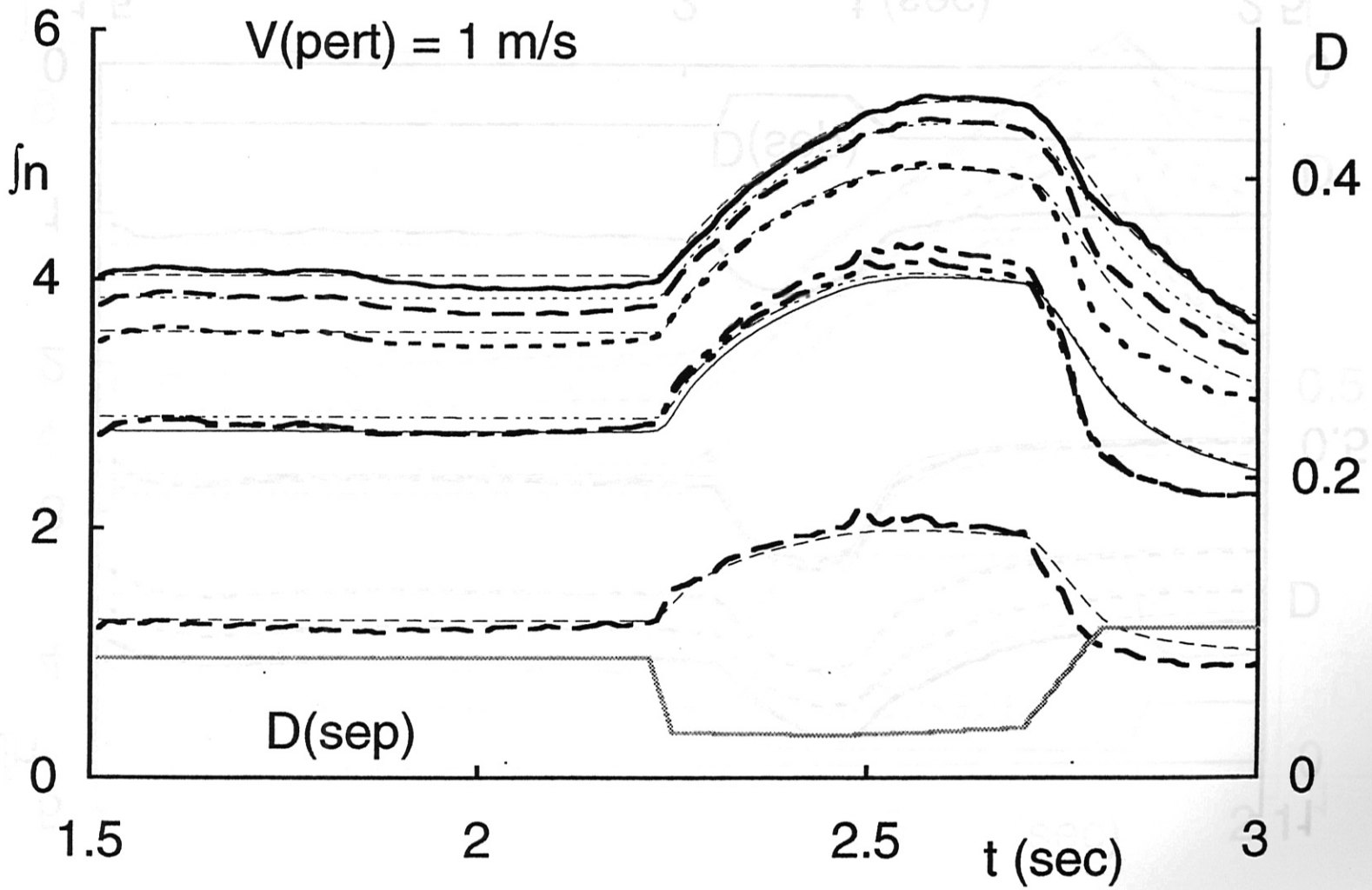

Fig. 11

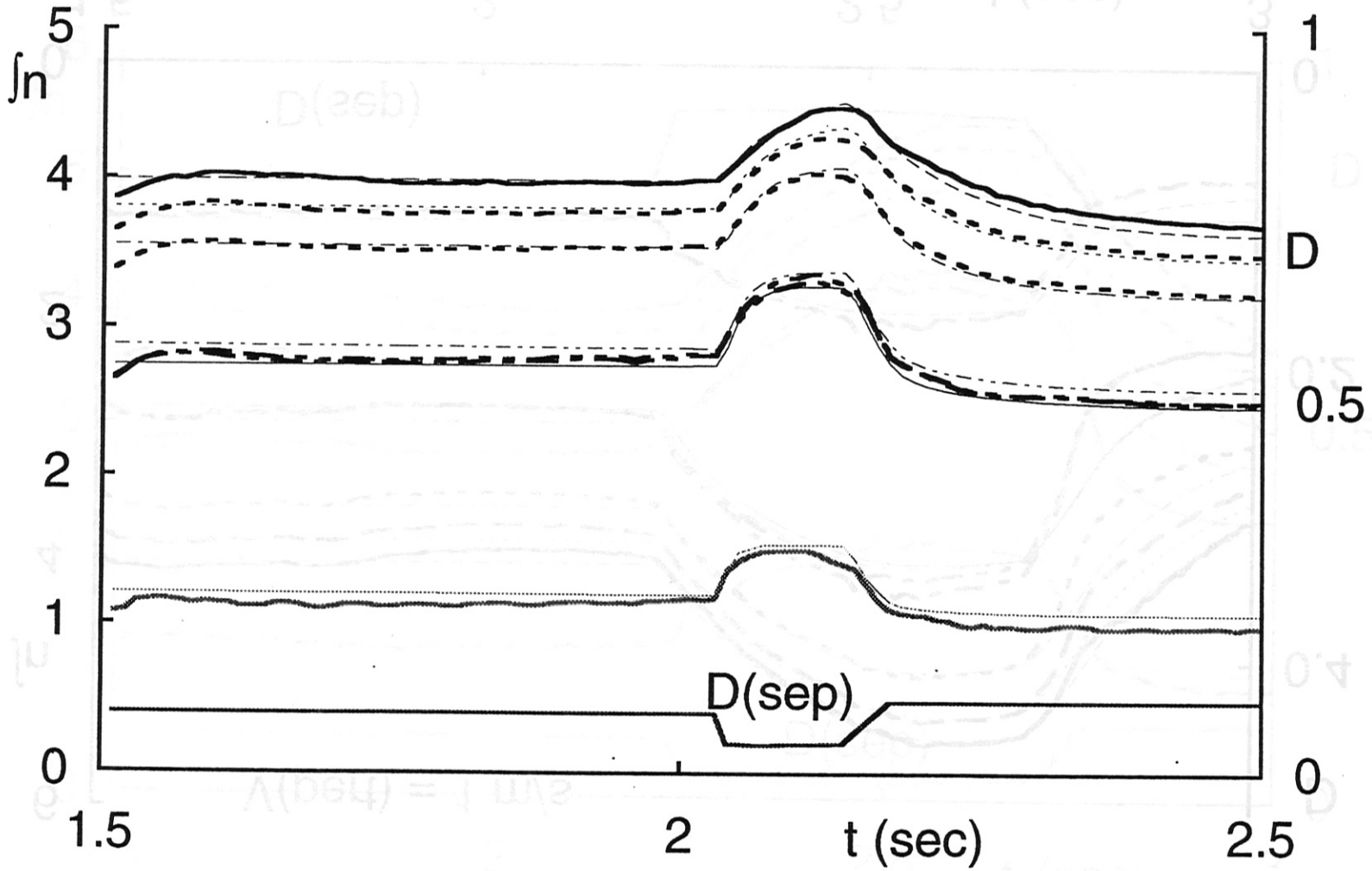

Fig. 12

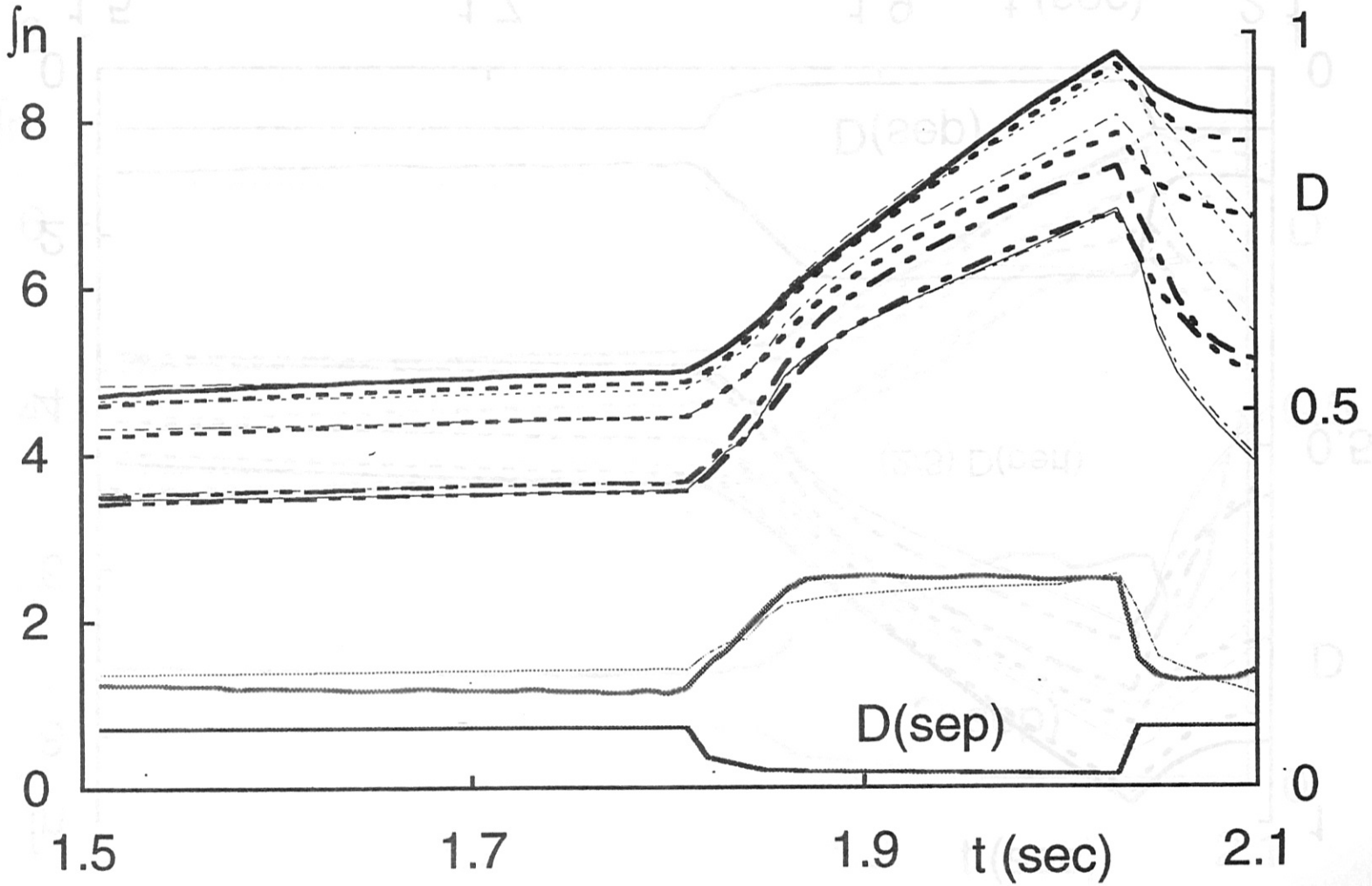

Fig. 13

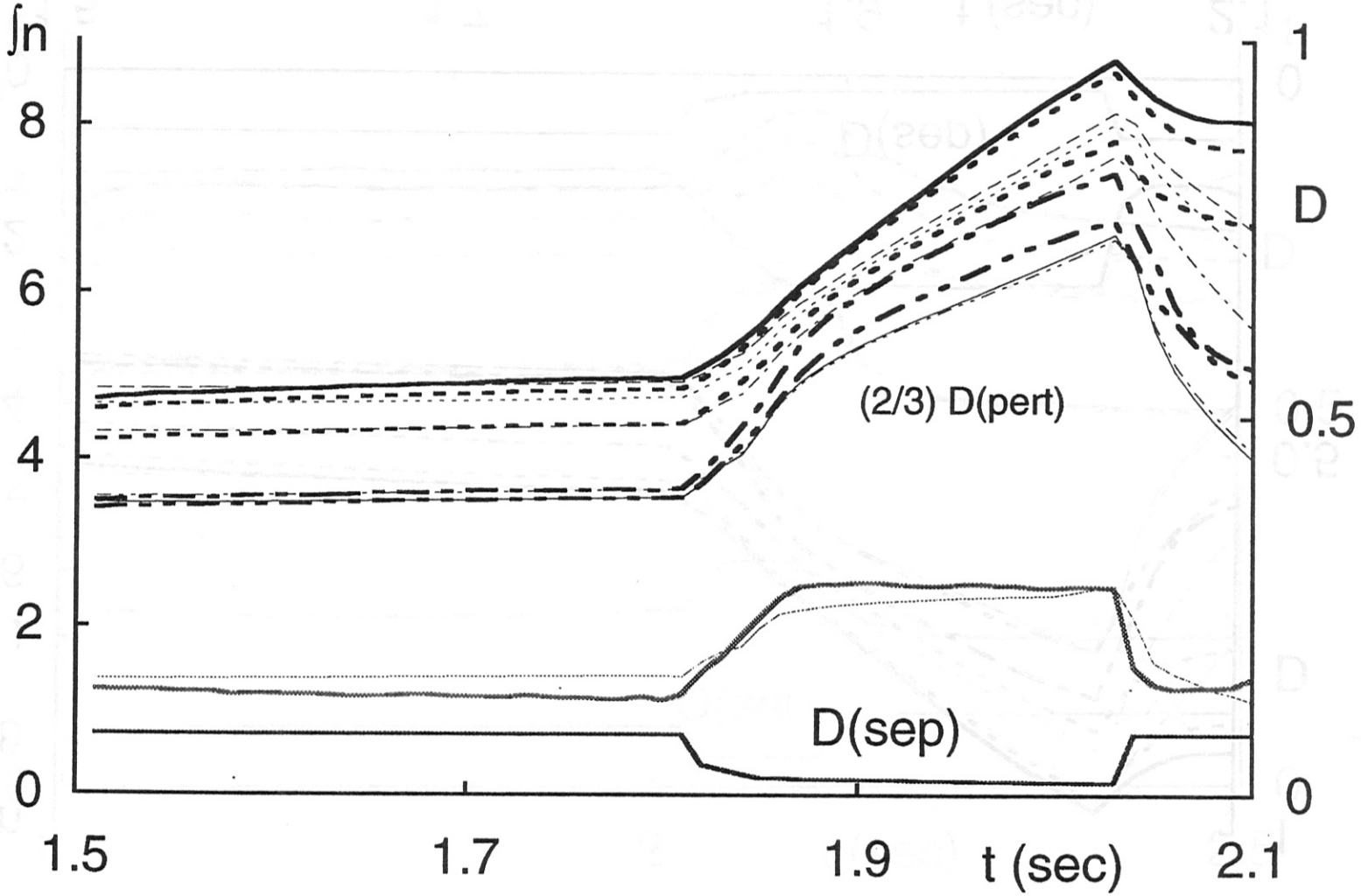

Fig. 14

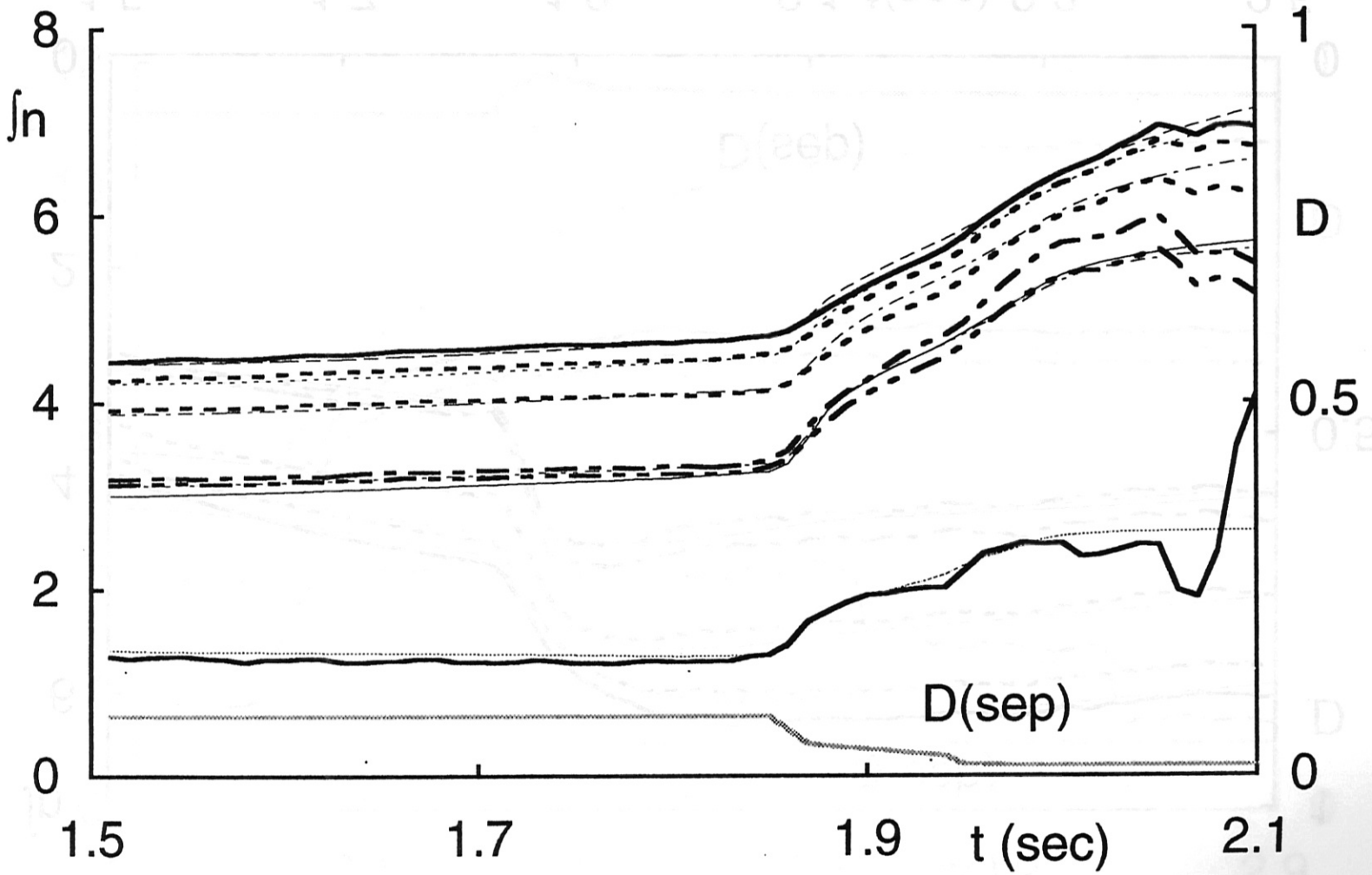

Fig. 15

A3496.CHT2;16

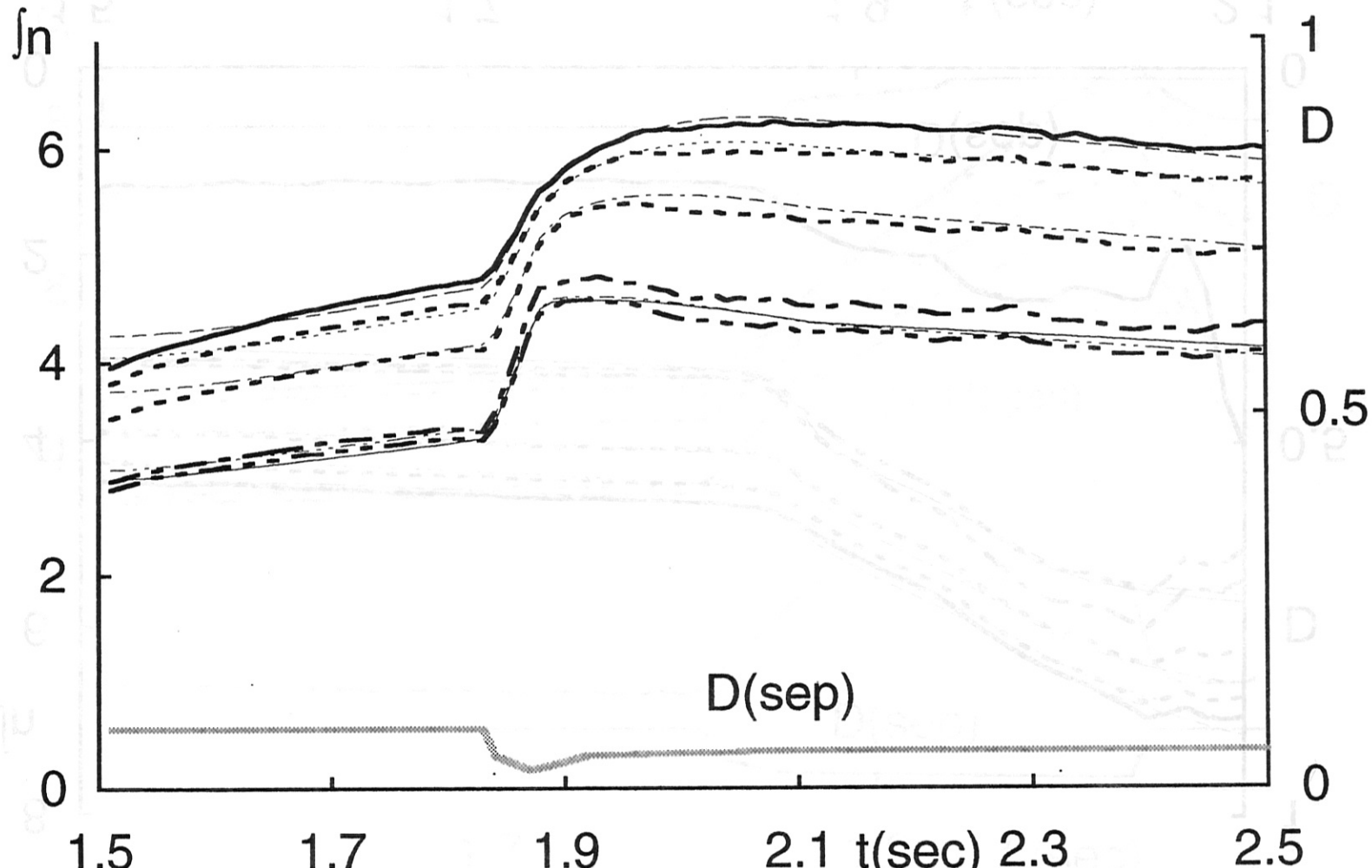

Fig. 16

A3703.CHT2;17

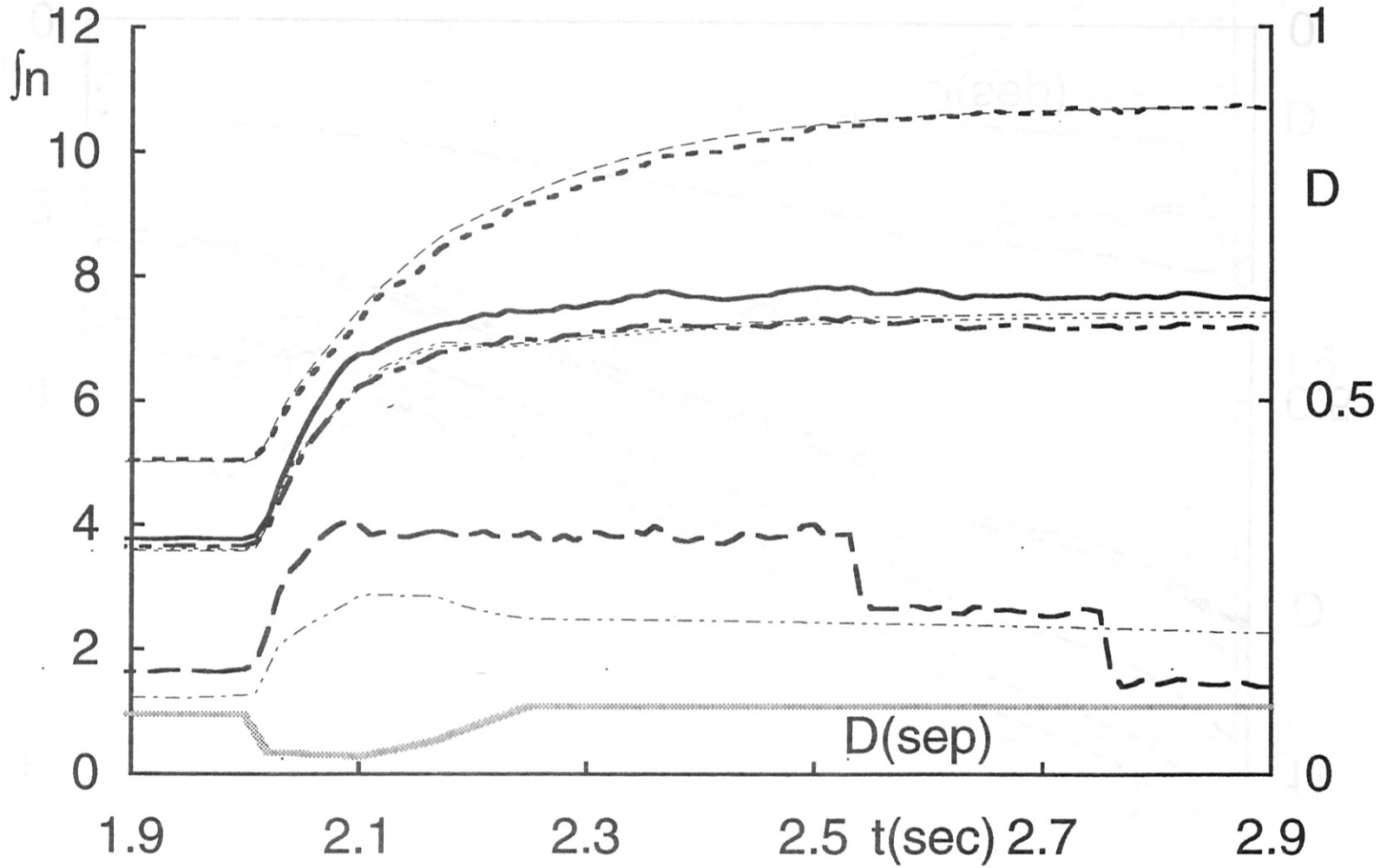

Fig. 17

A3674.CHT1;18

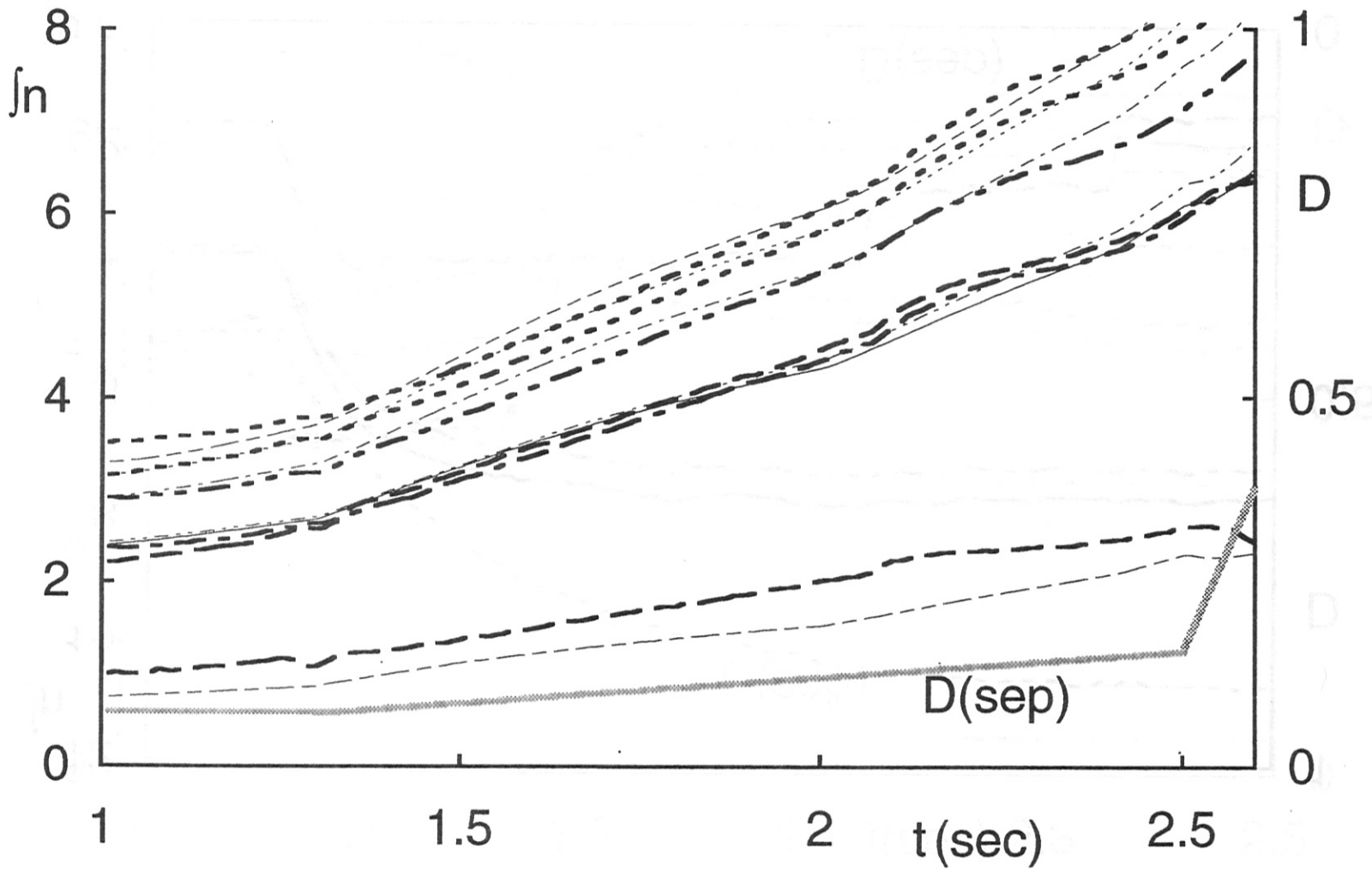

Fig. 18

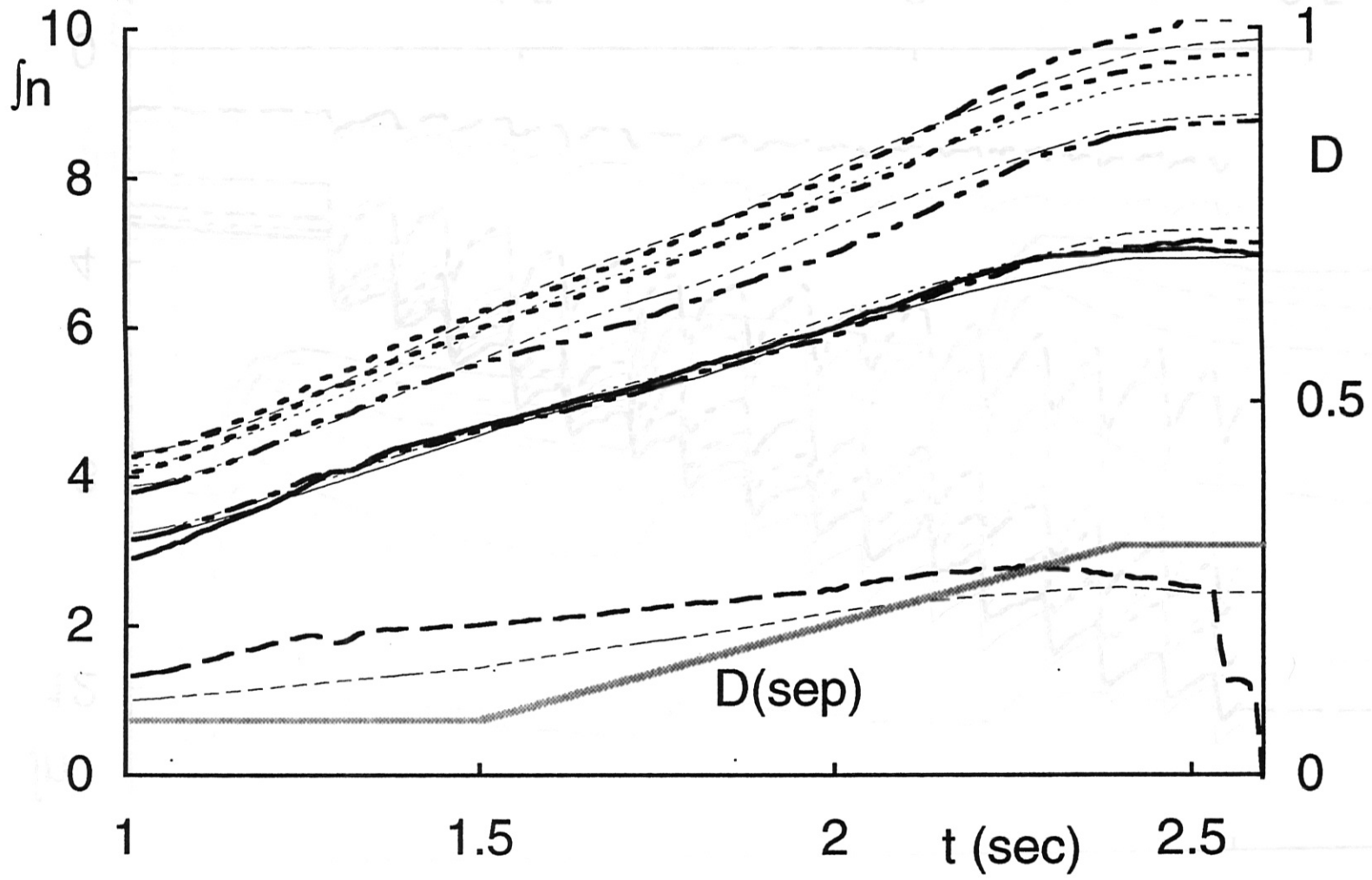

Fig. 19

A2725.CHTa;20

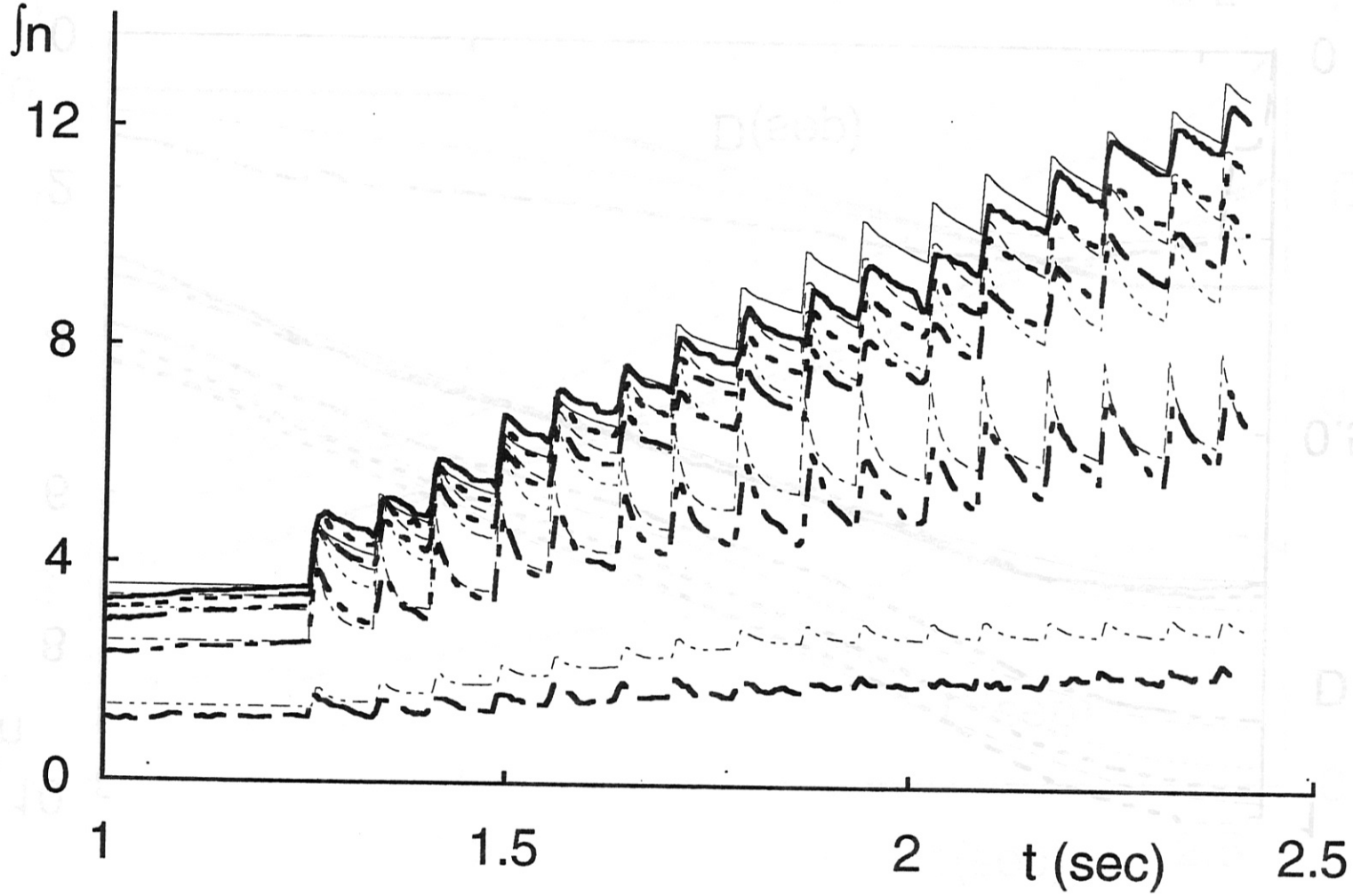

Fig. 20

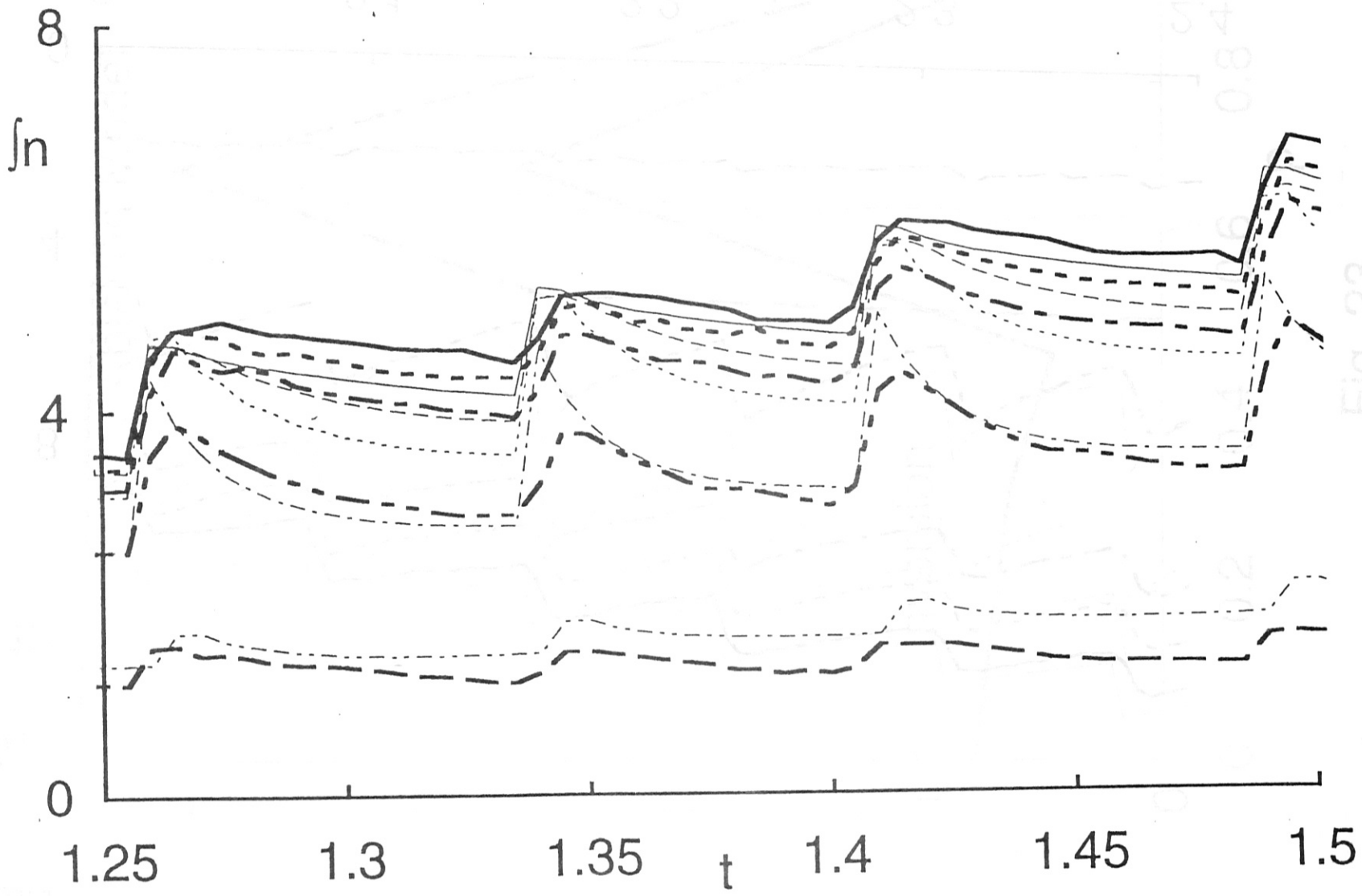

Fig. 21

A2725.CHTa;19

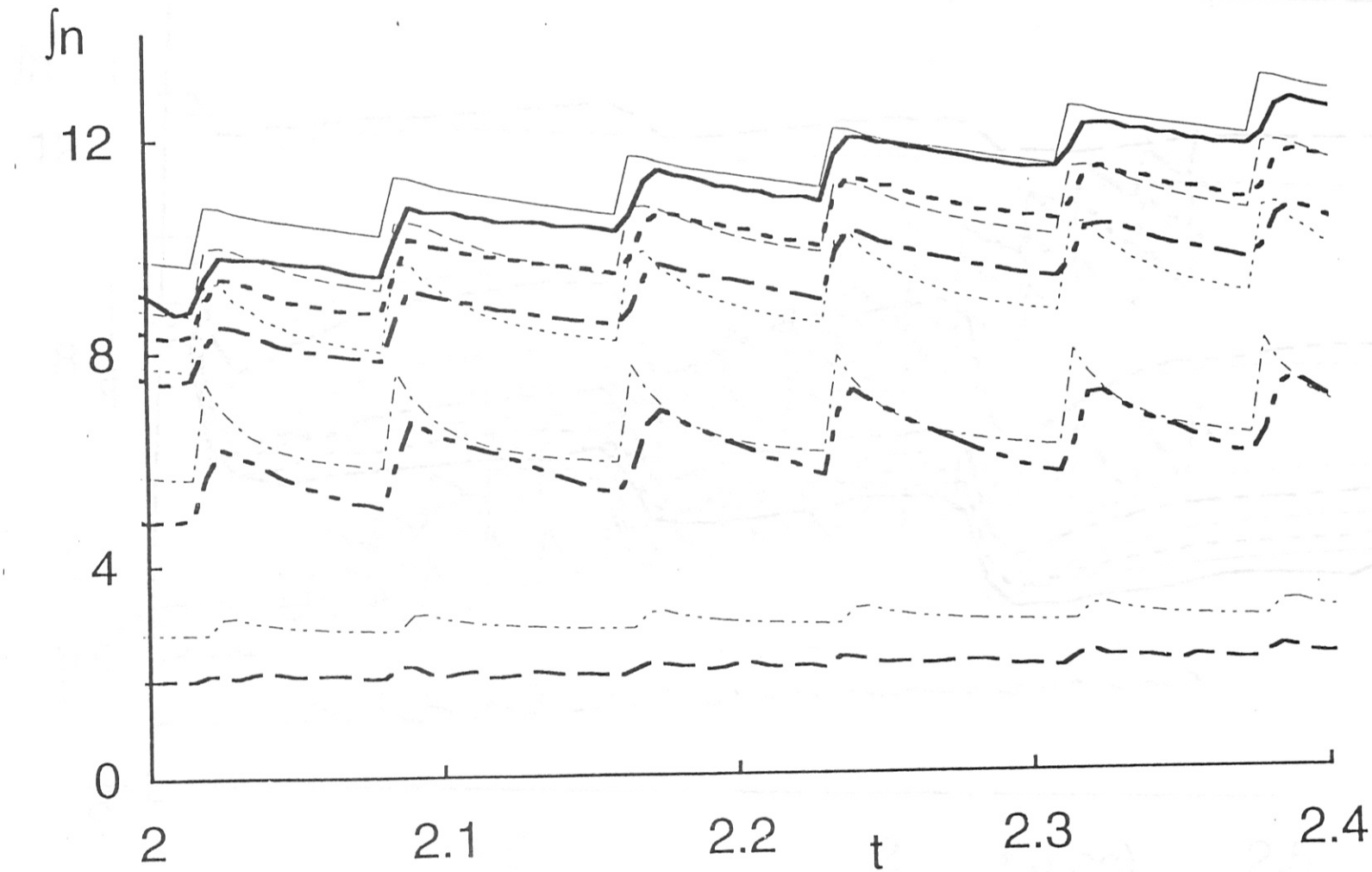

Fig. 22

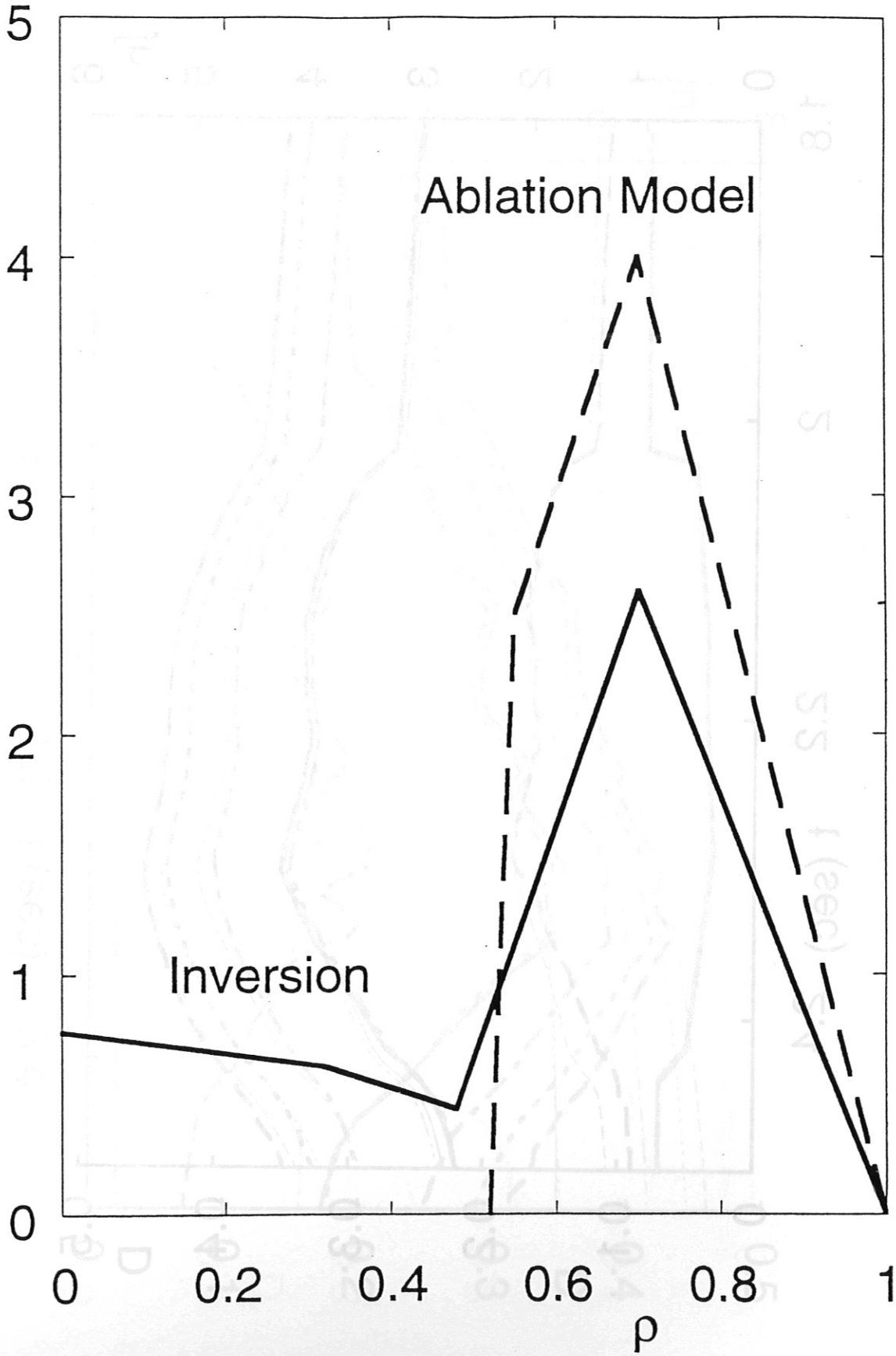

Fig. 23

A4741.CHT1;24

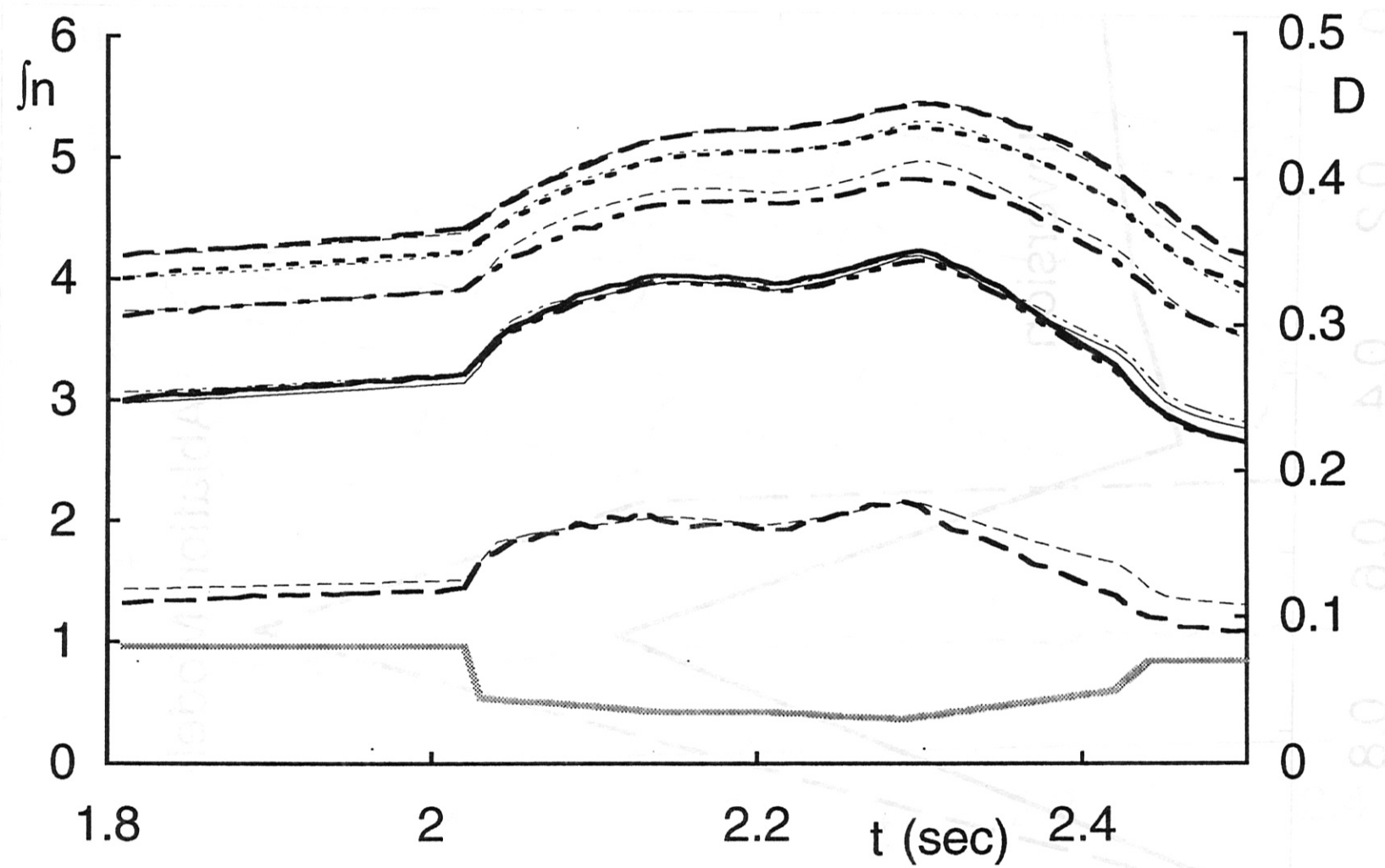

Fig. 24

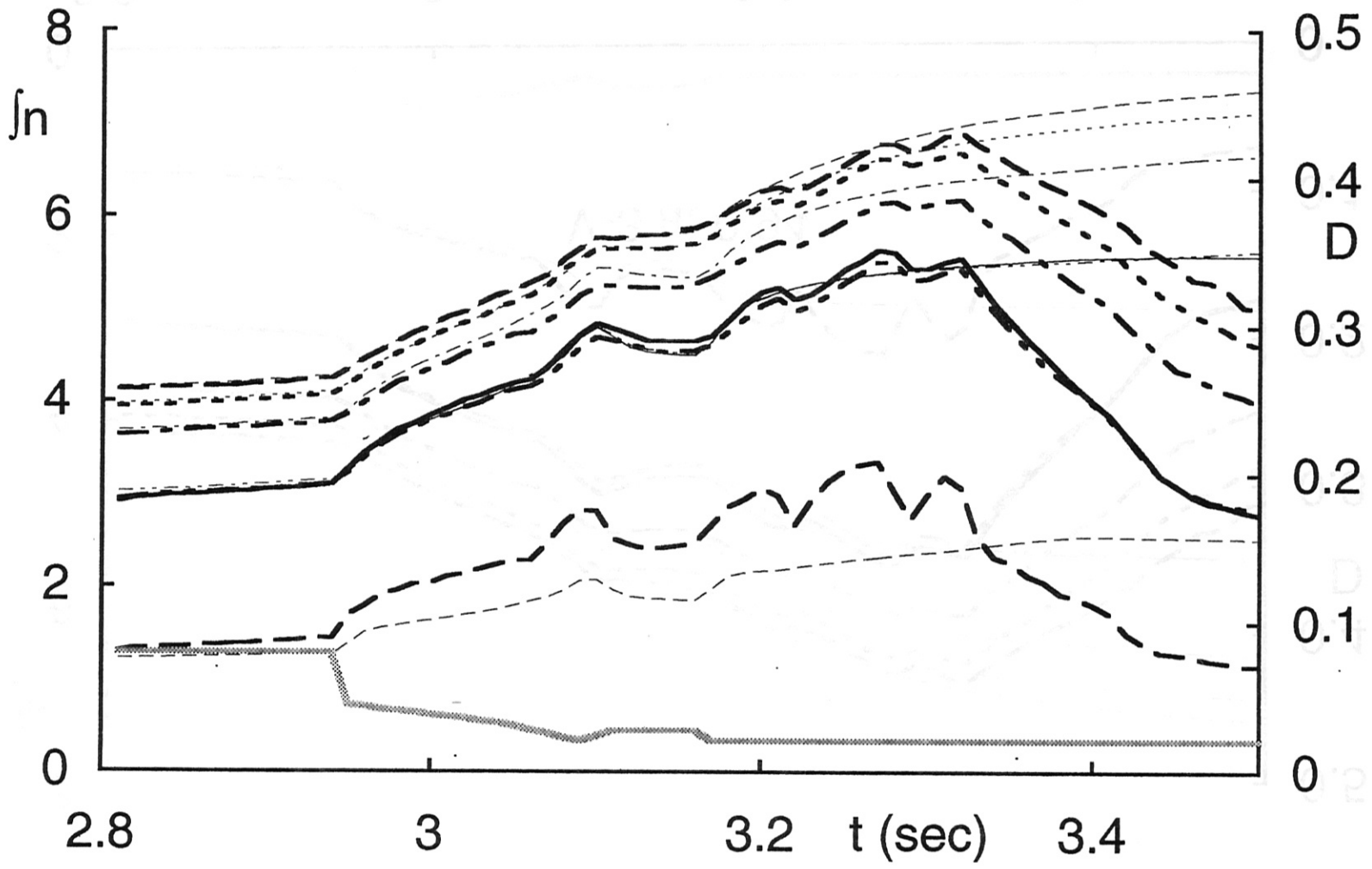

Fig. 25

A4744.CHT1a;26

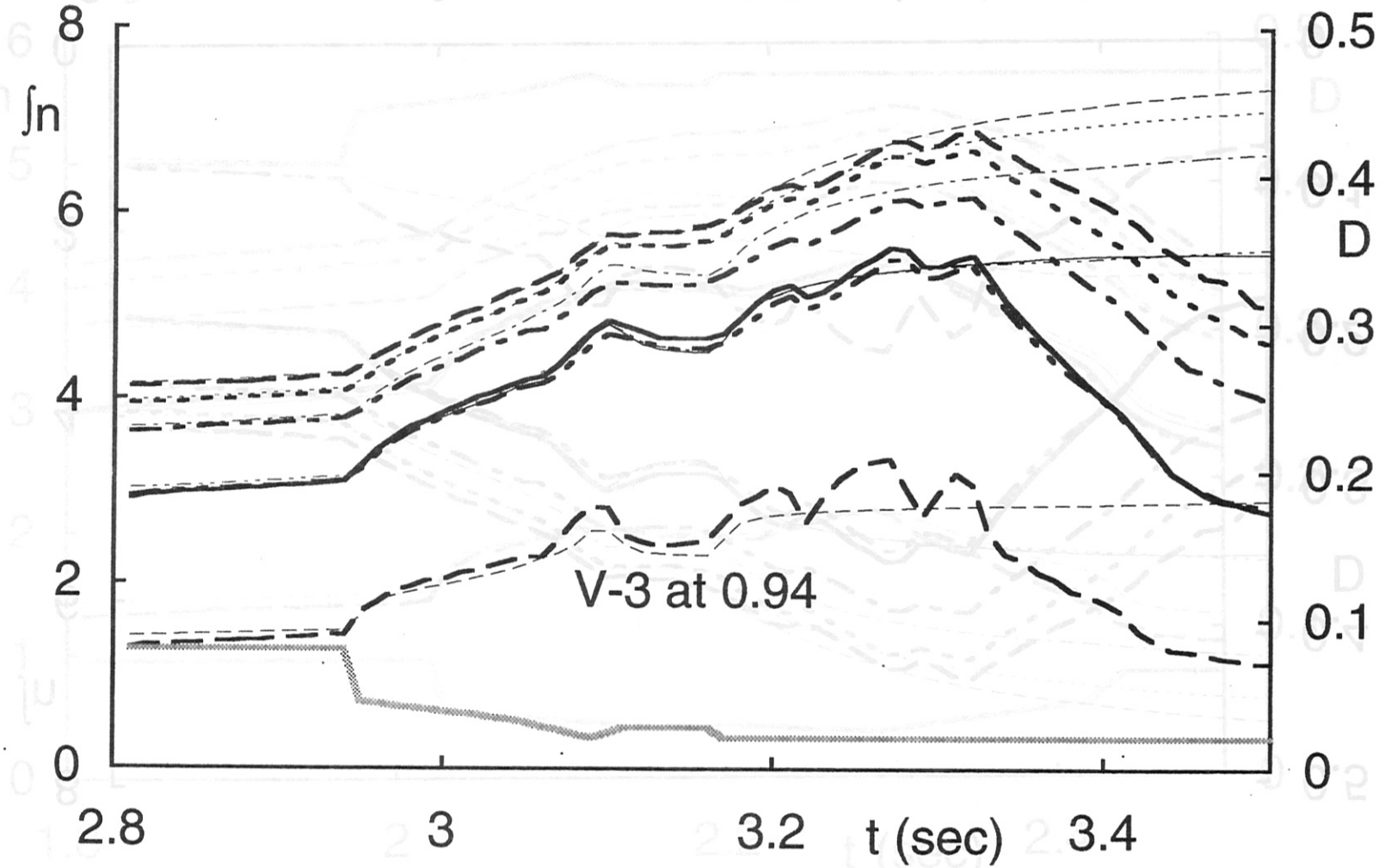

Fig. 26